haematologica
Journal of the Ferrata Storti Foundation

Selective lymphodepletion underlies the efficacy of horse anti-thymocyte globulin-based immunosuppressive therapy in aplastic anemia

by Emma S. Pool, Cilia R. Pothast, Shannah M. Gennesse, Esther H.M. van Egmond, Julia M. Giezen, Sabrina A.J. Veld, René E.M. Toes, Frits Koning, Constantijn J.M. Halkes, Mirjam H.M. Heemskerk, Dirk Jan A.R. Moes and Jennifer M-L. Tjon

Received: October 3, 2025.
Accepted: January 21, 2026.

Citation: Emma S. Pool, Cilia R. Pothast, Shannah M. Gennesse, Esther H.M. van Egmond, Julia M. Giezen, Sabrina A.J. Veld, René E.M. Toes, Frits Koning, Constantijn J.M. Halkes, Mirjam H.M. Heemskerk, Dirk Jan A.R. Moes and Jennifer M-L. Tjon. Selective lymphodepletion underlies the efficacy of horse anti-thymocyte globulin-based immunosuppressive therapy in aplastic anemia. Haematologica. 2026 Jan 29. doi: 10.3324/haematol.2025.300002 [Epub ahead of print]

Selective lymphodepletion underlies the efficacy of horse anti-thymocyte globulin-based immunosuppressive therapy in aplastic anemia

Authors

Emma S. Pool[1], Cilia R. Pothast[1], Shannah M. Gennesse[1], Esther H.M. van Egmond[1], Julia M. Giezen[2], Sabrina A.J. Veld[1], René E.M. Toes[2], Frits Koning[3], Constantijn J.M. Halkes[1], Mirjam H.M. Heemskerk[1], Dirk Jan A.R. Moes[4] and Jennifer M-L. Tjon[1]

[1] Department of Hematology, Leiden University Medical Center, Leiden, The Netherlands
[2] Department of Rheumatology, Leiden University Medical Center, Leiden, The Netherlands
[3] Department of Immunology, Leiden University Medical Center, Leiden, The Netherlands
[4] Department of Clinical Pharmacy and Toxicology, Leiden University Medical Center, Leiden, The Netherlands

Running head: Immunological effects of ATGAM-based IST in AA

Correspondence

Jennifer M-L. Tjon, MD PhD
Department of Hematology
Leiden University Medical Center
Albinusdreef 2
PO Box 9600
2300 RC Leiden
The Netherlands
Email: j.m.l.tjon@lumc.nl

Data-sharing statement

Pharmacokinetic and spectral flow cytometry data acquired in this study are available from the corresponding author upon reasonable request. Contact: Jennifer M-L Tjon, MD PhD; j.m.l.tjon@lumc.nl.

Acknowledgements

We thank the Laboratory for Special Hematology of the Leiden University Medical Center for processing all plasma samples. Furthermore, we thank Anja Jansen-Hoogendijk of the Department of Pediatrics of the Leiden University Medical Center for sharing her expertise on measuring active ATG concentrations in patient plasma. Flow cytometry was performed at the Flow Cytometry Core Facility of the Leiden University Medical Center. This work was supported by a research grant from Dioraphte Foundation.

Authorship contributions

E.S.P., C.R.P., S.M.G., E.H.M.v.E., J.M.G. and S.V. performed laboratory experiments. E.S.P. and D.J.A.R.M. performed pharmacokinetic modelling. E.S.P. analyzed the data. E.S.P., E.H.M.v.E., J.M.G., R.E.M.T, F.K., C.J.M.H., M.H.M.H., D.J.A.R.M. and J.M-L.T. interpreted the data. E.S.P wrote the first draft of the manuscript. C.J.M.H. and J.M-L.T. recruited patients and collected samples. D.J.A.R.M and J.M-L.T. conceptualized the study. M.H.M.H., D.J.A.R.M. and J.M-L.T. supervised the project. All authors critically reviewed the manuscript.

Conflicts of interest

The authors declare no competing financial interests.

Abstract

Horse-derived anti-thymocyte globulin (ATGAM) in combination with long-term ciclosporin is the first-line treatment for most immune-mediated aplastic anemia (AA) patients. The exact impact of this immunosuppressive therapy (IST) on hematological recovery and the immune landscape, however, remains poorly understood. We report a longitudinal analysis of the pharmacodynamic effects of ATGAM-based IST in a cohort of 44 AA patients. With flow cytometry we quantified plasma levels of lymphocyte-binding ATGAM, which is believed to mediate the therapeutic effect. Population pharmacokinetic modeling revealed substantial between-patient variability in ATGAM exposure, with higher exposure levels associating to earlier hematologic recovery. ATGAM bound all lymphoid lineages and profoundly depleted T- and NK-cells at high plasma concentrations. Strikingly, ATGAM did not deplete B-cells but instead induced an increase of $CD27^{+}$ B-cells. Deep immunophenotyping on series of peripheral blood samples collected up to three years after start of IST demonstrated that ATGAM induced rapid depletion of T-cells, including $KLRG1^{+}$ terminally differentiated $CD8^{+}$ T-cells and Th17-like $CCR6^{+}CD4^{+}$ T-cells. Although naïve and pathogen-specific T-cells were also depleted, they recovered quickly, indicating preservation of protective immunity. Notably, $CCR6^{++}$ B-cells, implicated in AA pathogenesis, escaped ATGAM depletion but reduced gradually over time along with residual potentially pathogenic T-cells, including the $CCR6^{+}CD4^{+}$ T-cells. This could explain the crucial contribution of long-term ciclosporin to successful IST. Collectively, our results identify ATGAM exposure as a factor influencing hematologic recovery, and indicate that the therapeutic effect of IST goes beyond total lymphodepletion but is rather the result of selective depletion and suppression of key lymphocyte subpopulations.

Introduction

Immune-mediated aplastic anemia (AA) is a bone marrow failure syndrome caused by an autoimmune attack on the hematopoietic stem and progenitor cells (HSPCs)[1]. The resulting peripheral cytopenias can lead to severe bleeding and infections. Effective treatments are allogeneic hematopoietic stem cell transplantation (allo-HSCT) or immunosuppressive therapy (IST). IST is the first-line treatment for most patients due to older age or lack of a matched donor[2].

Standard first-line IST for AA combines anti-thymocyte globulin (ATG) with long-term ciclosporin. ATG is a polyclonal antibody mixture that can be produced by immunizing horses or rabbits with human thymocytes. In AA, both horse-derived ATG (ATGAM®, Pfizer) and rabbit-derived ATG (Thymoglobulin®, Sanofi) have been applied. However, ATGAM is preferred since it results in superior response rates and overall survival[3, 4]. Approximately 70% of patients show hematologic recovery after ATGAM-based IST, with a gradual improvement of peripheral blood counts over several months[2, 4, 5].

The pharmacodynamics of ATGAM-based IST are poorly understood. Its therapeutic effect is attributed to the depletion of autoreactive immune cells implicated in AA pathogenesis. ATGAM, administered at 40mg/kg/day for four consecutive days[2], is thought to induce immediate lymphodepletion, possibly through complement-dependent lysis or activation-induced apoptosis[6, 7]. Subsequently, long-term ciclosporin is believed to suppress residual and reconstituted lymphocytes through calcineurin and IL-2 blockade[8, 9]. Since ATGAM is manufactured in horses, it contains antibodies against both non-human and human antigens. Therefore, only a small 'active' fraction can bind human immune cells and mediate its immunomodulatory effects. The precise specificities of this active ATGAM fraction are unknown and its activity differs from the more extensively studied rabbit-derived ATG[7, 10], however, ATGAM has been shown to bind a spectrum of proteins on the surface of immune cells[11, 12], and to reduce $CD4^+$, $CD8^+$ and regulatory T-cells *in vivo*[4, 13]. Similarly, the relationship between active ATGAM exposure and lymphodepletion is unclear, and the impact of ATGAM plus ciclosporin on the immune landscape has not been characterized in detail. Previously, we identified potentially pathogenic T- and B-cell subpopulations in AA patients[14, 15]. These $CCR6^{++}$ B-cells, Th17-like $CCR6^+CD4^+$ T-cells and $KLRG1^+$ terminally differentiated $CD8^+$ T-cells were enriched at diagnosis, colocalized in bone marrow, and significantly reduced six months post-ATGAM. This decrease could imply that IST selectively depletes specific lymphocyte subpopulations.

In this study, we aimed to delineate the effects of ATGAM exposure on hematologic recovery in 44 AA patients. For the first time, we quantified active ATGAM concentrations in

patient plasma using flow cytometry, and applied population pharmacokinetic (POPPK) modeling to estimate exposure. Furthermore, to elucidate the impact of IST with ATGAM plus ciclosporin on the immune landscape, we performed spectral flow cytometry on peripheral blood samples collected before and at multiple time points after start of IST. Our results present active ATGAM exposure as a factor influencing hematologic recovery and reveal that successful IST involves selective removal and suppression of key lymphocyte subpopulations rather than a full immune 'reset'.

Methods

Patients and plasma samples

Plasma samples (n=381) were collected from 44 treatment-naïve AA patients before each ATGAM infusion and up to 82 days after the first infusion (median 9, range 4-13 samples/patient). PBMCs were collected from 3 of 44 patients at diagnosis and up to 3.5 years post-ATGAM (7-10 samples/patient), and 5 healthy donors. Patient characteristics are listed in **Table 1**. Patients <40 years were screened for Fanconi anemia to exclude congenital bone marrow failure. Patients received IST according to Dutch guidelines: four consecutive days 40mg/kg/day ATGAM and 5mg/kg/day ciclosporin for at least six months[16]. Exceptions were UPN5 (two days ATGAM), UPN9 (four days ATGAM with two-day break after infusion two), and UPN46 (118 days ciclosporin). ATGAM was administered intravenously over 12 hours. 19 of 44 patients responded within six months after start of IST, which was defined as becoming transfusion-independent and a neutrophil count of $\geq 0.5 \cdot 10^9/L$[2]. Plasma or PBMCs were stored at -80°C or -196°C until bioanalysis, respectively. This study was approved by the Medical Ethical Committee of the Leiden University Medical Center (B21.003).

ATGAM measurement and spectral flow cytometry

Flow cytometry was used to quantify active ATGAM concentrations in plasma, and to perform deep immunophenotyping in peripheral blood. For active ATGAM measurement, cryopreserved PBMCs from a single healthy donor were incubated with serial dilutions of patient plasma using a protocol based on a previously validated assay for quantifying lymphocyte-binding antibody concentrations[17], and stained with a six-marker antibody panel including anti-horse IgG. Subsequently, cells were measured by flow cytometry, and active ATGAM plasma concentrations were determined. For deep phenotyping of lymphocytes, cryopreserved PBMC samples were stained with a 25-marker panel (**Table S1**), measured by spectral flow cytometry, and analyzed by dimensionality reduction[18]. Detailed description of all methods, including the quantification of total ATGAM in plasma by ELISAs, is provided in the **Supplementary methods** and **Figures S1-3**.

Exposure-response analyses

POPPK modelling was performed in NONMEM® to estimate ATGAM exposure as detailed in **Supplementary methods, Tables S2-3** and **Figure S4**. Downstream exposure-response analyses used clinical data collected until day 180, because IST-response is assessed 3-6 months post-ATGAM[2]. As a measure for hematologic recovery, we evaluated peripheral blood neutrophil and reticulocyte counts from routine measurements, generally taken at least weekly. Thrombocyte and hemoglobulin levels were not analyzed to avoid potential bias caused by blood transfusions. To study lymphodepletion and immune reconstitution, we analyzed peripheral blood lymphocyte counts from routine measurements, typically collected once every two weeks. To correct for missing immune reconstitution data, non-linear mixed effect modeling was performed using SAEMIX[19], see **Supplementary methods** and **Figure S5**. Data visualization and statistical analyses were performed in R v4.4.1 (Rstudio v2023.03) using Mann-Whitney *U* (continuous variables), Fisher's Exact (categorical variables), and Spearman's correlation tests. P-values ≤0.05 were considered significant.

Results

Active ATGAM binds all major lymphoid lineages

To study the effects of ATGAM, the concentration of ATGAM capable of binding PBMCs from an unrelated healthy donor (active ATGAM hereafter) was quantified in plasma from 44 adult AA patients using flow cytometry (**Figure 1A**). In patients that received the standard regimen of four consecutive days 40mg/kg/day ATGAM, active ATGAM concentrations increased over the four days of infusion and reached a median peak concentration of 131AU/mL on day 4 (**Figure 1B**). After the last infusion, concentrations rapidly decreased, and typically fell below the concentration of 10AU/mL by day 20. The pharmacokinetics of active ATGAM varied considerably between patients in both peak concentrations (range 31-497AU/mL on day 4) and clearance rates (**Figure 1B**). Similar variability was observed in total ATGAM concentrations (e.g. active ATGAM and ATGAM binding to other (non)-human targets combined) quantified in the same plasma samples using ELISA (**Figure S6A**). Active ATGAM in patient plasma was detected on donor T-, NK- and B-cells. However, pharmacokinetics differed as B-cell binding active ATGAM was detected longer than T- or NK-cell binding active ATGAM (**Figure 1C**; all patients in **Figure S6B**).

Active ATGAM exposure is increased in AA patients with higher body weight

Given the variability in active ATGAM concentrations between patients, POPPK modeling was performed to estimate the full concentration-time curve of active ATGAM exposure. The POPPK of intravenously administered active ATGAM were best described by a two-compartment model with first-order linear elimination (structural model in **Figure S7**).

The model showed adequate agreement between observed and model-estimated active ATGAM concentrations (**Figure S8**, individual patients in **Figure S9**). Exposure ($AUC_{0\text{-}inf}$) was defined as the estimated area under the concentration-time curve (**Table S4**). Since this study is the first to report on active ATGAM, we also validated the accuracy of our approach by performing POPPK modelling for total ATGAM (**Figure S10-11, Table S5**) to simulate the dosing regimens described in the manufacturer's brochure[20]. This revealed strong agreement between model-estimated and reported total ATGAM concentrations for an external cohort of AA patients (**Figure S12**).

To identify factors driving between-patient variability in active ATGAM pharmacokinetics, the impact of clinical covariates was evaluated. No significant effects of sex, age and lymphocyte counts pre-ATGAM were observed (**Figure S13**). Since ATGAM is dosed based on body weight, we anticipated clearance to increase with body weight to obtain similar ATGAM exposures across patients. However, we found that patients with higher body weights had higher active ATGAM concentrations in time, resulting in higher exposures (**Figure 1D**), as neither clearance nor volume of distribution were influenced by weight (**Figure 1E-F**).

Higher active ATGAM exposure associates with earlier hematologic recovery

To investigate the effect of active ATGAM exposure on hematological recovery, patients were categorized into low, medium and high exposure groups based on the exposure tertiles of 1515 and 2216AU·day/L (**Figure 2A**). Neutrophil and reticulocyte counts served as a measure for bone marrow recovery. Two patients in the low-exposure group, one patient in the medium-exposure group and one in the high-exposure group were censored before day 180 due to death. Age, sex, disease severity, eltrombopag use and ciclosporin discontinuation did not significantly differ between the groups, and none of the patients started second-line treatment before day 180 (**Table S6**). In all three exposure groups, neutrophil and reticulocyte counts gradually increased post-ATGAM (**Figure 2B-C**). Reticulocyte counts peaked in a few patients within the first 120 days post-ATGAM. Notably, the high- and medium-exposure groups tended to have higher neutrophil and reticulocyte counts from day 60 onward, despite similar baseline counts compared to the low-exposure group (**Figure 2B-C**). This difference was most pronounced around day 90 (**Figure 2B-C,** box plots) and diminished 180 days post-ATGAM infusion, suggesting that increased active ATGAM exposure associates with earlier hematologic recovery but does not impact six-month response rates.

ATGAM induces profound depletion of T- and NK-cells but not of B-cells

As we showed that ATGAM binds all major lymphoid lineages, we studied the response of active ATGAM exposure on T-, NK- and B-cell counts in peripheral blood. To correct for missing immune reconstitution data, total lymphocyte, T-cell and NK-cell counts were

estimated by non-linear mixed modelling. ATGAM induced a strong reduction of $CD4^+$ T-cells, $CD8^+$ T-cells and NK-cells, with no differences between the active ATGAM exposure groups (**Figure 2D**). Depletion of these lineages was short-lived and only observed immediately post-infusion, suggesting that T- and NK-cell depletion requires a minimal active ATGAM plasma concentration (+/-100AU/mL, estimated from **Figure 2D**). Strikingly, B-cell counts did not show a consistent trend between patients post-ATGAM and therefore could not be modelled. Interestingly, B-cell counts even peaked post-ATGAM before returning to baseline around day 30, indicating that although ATGAM binds all lymphoid lineages, it exerts differential effects among cell types.

Detection of ATGAM on patient lymphocytes confirms B-cell binding *in vivo*

To study the paradox that ATGAM binds donor B-cells but does not induce B-cell depletion, we investigated the presence of ATGAM directly bound to patient PBMCs. Unique series of PBMC samples collected from three AA patients before and immediately after ATGAM infusion were studied. A 25-marker spectral flow cytometry panel including anti-horse IgG enabled the detection of ATGAM on the surface of in-depth phenotyped lymphocytes. To study the long-term effects of ATGAM plus ciclosporin, samples collected up to 3.5 years post-ATGAM were also analyzed (total of 7-10 samples/patient). Patients received 40mg/kg/day ATGAM on four consecutive days, responded to IST (peripheral blood counts in **Figure S14**) and were CMV seropositive. Ciclosporin was discontinued after tapering two years post-ATGAM in patient UPN31, and three years post-ATGAM in UPN13 and UPN15. As a reference, PBMCs from five age-, sex- and CMV status-matched healthy donors were included.

To directly compare the immune landscape between time points, UMAPs were generated after downsampling $0.1 \cdot 10^6$ single, live lymphocytes from each sample (**Figure 3A**). The following major lymphoid lineages were identified: 1) $CD3^+CD4^+$ T-cells; 2) $CD3^+CD8^+$ T-cells; 3) $CD3^+TCR\gamma\delta^+$ T-cells; 4) $CD3^+CD4^+FoxP3^+$ regulatory T-cells; 5) $CD3^-CD56^+$ NK-cells and 6) $CD19^+$ B-cells. Visualization of all samples from a representative patient in the UMAP revealed a shift in the lymphoid compartment over time, with the most obvious changes observed immediately after the last ATGAM infusion on day 4, when T-cells and NK-cells were reduced but B-cells were still present (**Figure 3B**).

Quantification of lineage frequencies confirmed the presence of the major lymphoid lineages at AA diagnosis, with some heterogeneity between patients and no considerable differences compared to controls (**Figure 3C,** $TCR\gamma\delta^+$ and regulatory T-cells in **Figure S15A**). Immediately after the last ATGAM infusion (day 4/5) the composition of the lymphoid compartment changed dramatically. In agreement with previous observations, percentages of $CD4^+$, $CD8^+$, $TCR\gamma\delta^+$ and regulatory T-cells and NK-cells decreased in all patients, whereas

B-cell frequencies increased. A trend towards normalization was observed from two weeks post-ATGAM onwards. Normalization of the lymphoid compartment continued up to six months post-ATGAM.

With anti-horse IgG, ATGAM was best detectable on day 4, and could be detected until day 26 on all circulating lymphocytes from the representative patient post-infusion (**Figure 3B,D**). The amount of ATGAM bound to T-cells or B-cells did not differ (**Figure S15B**). To rule out a potential influence of ATGAM Fc-binding to the Fc-receptor on B-cells, Fc-receptor blockade experiments were performed and no Fc-binding was found (**Figure S16**). ATGAM binding to patient lymphocytes gradually decreased within one month post-infusion. Lower concentrations of ATGAM again correlated with T- and NK-cell recovery from two weeks post-infusion onwards. These findings confirm that while ATGAM binds to all lymphoid lineages, it does not induce B-cell depletion to the same extent as observed in T- and NK-cells.

ATGAM profoundly depletes memory T-cells but induces an increase of CD27$^+$ B-cells

Next, we studied the immediate effects of ATGAM and long-term impact of ATGAM plus ciclosporin at the immune subpopulation level. In the representative patient, we observed a more profound decrease of memory T-cells compared to naïve T-cells post-ATGAM, with the strongest depletion of CD45RA$^+$CCR7$^-$ terminally differentiated effector memory (EMRA) CD8$^+$ T-cells (**Figure 4A-B,** quantification: **Figure S15C-D**). In contrast, we observed a striking increase of memory CD27$^+$ B-cells immediately post-ATGAM (**Figure 4C, S15E**).

The profound depletion of memory T-cells and increase of memory CD27$^+$ B-cells was observable across all patients post-ATGAM (**Figure 5A-C**). Only in patient UPN15 memory T-cell frequencies remained high, which was attributable to the low number of analyzed T-cells, as this patient experienced the strongest T-cell depletion (**Figure 3C**). Within two weeks post-ATGAM, both memory T-cells and CD27$^+$ B-cells frequencies showed a trend towards normalization (**Figure 5A-C**). Notably, this normalization occurred independently of T-cell and B-cell proliferation, indicating that recovery was not driven by proliferation of remaining circulating cells (**Figure S17**).

To further characterize the increase of CD27$^+$ B-cells, we examined the identity of these cells in patient UPN31 on day 13 using a B-cell-oriented spectral flow cytometry panel. This revealed that the CD27$^+$ B-cells comprised of a heterogeneous population of both unswitched (IgM$^+$IgD$^+$) and switched (IgG$^+$, IgA$^+$) memory B-cells (**Figure 5D**). Compared to healthy controls, these cells preserved high levels of CD21 and CD24, compatible with a resting B-cell state (**Figure 5E**). Additionally, they did not differentially express the activation markers CD80, CD86 and CD95, and complement inhibitors CD46 and CD55 (**Figure 5E-F**), illustrating

that the increase of $CD27^+$ B-cells is not the result of cell expansion or resistance to complement-mediated lysis. Consistent with these findings, the $CD27^+$ B-cells harbored tetanus-specific cells, indicating their increase was driven by a recruitment of resting, pre-existing memory B-cells in circulation (**Figure 5G**).

ATGAM-based IST depletes potentially pathogenic subpopulations while allowing the recovery of virus-specific lymphocytes

The rapid recovery of the T-cell compartment in the absence of proliferation, along with the persistence of pre-existing memory B-cells post-ATGAM, raises the question of how profoundly ATGAM depletes the T-cell compartment. Therefore, we investigated the origin of reconstituted T-cells by tracking the presence of CMV-specific $CD8^+$ T-cells using CMV peptide-HLA tetramers incorporated into our spectral flow cytometry panel. In one of three patients (UPN13), these analyses were not possible due to HLA-incompatibilities between the patient and the tetramers. In the representative patient (UPN31), we detected CMV-specific $CD8^+$ T-cells at diagnosis, which were no longer detectable immediately following ATGAM infusion, consistent with the observed T-cell depletion (day 4; **Figure 6A**). However, CMV-specific $CD8^+$ T-cells were detectable from day 13 onwards, and a similar trend was observed in UPN15 (**Figure 6B**).

Given that our results indicate the persistence of pre-existing T- and B-cells post-ATGAM, we reasoned that the therapeutic effect of IST, comprising ATGAM and long-term ciclosporin, may not depend on a full immune 'reset'. Instead, it may rely on the selective depletion and suppression of pro-inflammatory $CCR6^{++}$ B-cells, $CCR6^+$ memory $CD4^+$ T-cells and $KLRG1^+$ EMRA $CD8^+$ T-cells, which we previously identified as part of a disease-specific immune cell network[14]. These subpopulations were enriched in AA patients at diagnosis, and co-localized in bone marrow regions harboring the active immune response[14, 15]. In all three patients, we confirmed higher frequencies of $CCR6^{++}$ B-cells at diagnosis compared to controls (**Figure 6C**). CCR6 expression on B-cells remained high immediately post-ATGAM but gradually decreased with long-term ciclosporin use, with the strongest decrease in CCR6 expression >6 months post-ATGAM. CCR6 expression remained reduced after ciclosporin was discontinued (≥3 years post-ATGAM). A similar decrease of CCR6 expression on $CCR6^+$ memory $CD4^+$ T-cells was observed (**Figure 6D**). In contrast, $KLRG1^+$ EMRA $CD8^+$ T-cells were strongly depleted immediately post-ATGAM (**Figure 6E**), and their recovery was delayed compared to other $CD8^+$ T-cells (**Figure 3C**). Further analysis showed that only a small fraction of these $KLRG1^+$ EMRA $CD8^+$ T-cells were CMV-specific, suggesting depletion also affected potentially autoreactive T-cells within this population (**Figure 6F**). Over time, $KLRG1^+$ EMRA $CD8^+$ T-cell frequencies returned to pre-ATGAM levels, indicating a temporary rather than a permanent depletion. A depletive effect was also observed for Granzyme B^+ cytotoxic T-cells (**Figure 6G**), while expression of the activation marker CD38 remained unaffected by ATGAM

plus ciclosporin (**Figure 6H**). These findings underscore that IST results in an immediate but selective depletion of key T-cell populations by ATGAM, while other potentially pathogenic populations are reduced over several months, possibly through selective suppression by ciclosporin.

Discussion

In this study, we investigated the pharmacodynamics of first-line IST with ATGAM plus long-term ciclosporin in AA patients. Our analysis is the first to focus on active ATGAM, the fraction capable of binding human lymphocytes and mediating the immunomodulatory effects that are believed to underly its therapeutic efficacy. POPPK modeling revealed that active ATGAM exposure varies considerably among patients, and tends to correlate with hematologic recovery. At high plasma concentrations, ATGAM binds T- and NK-cells and drastically reduces their counts *in vivo*. Paradoxically, while ATGAM also binds B-cells, it does not induce their depletion but rather results in an increase of resting memory $CD27^+$ B-cells in circulation. Following ATGAM infusion, immune reconstitution occurs rapidly within two weeks, and is marked by the recovery of pre-existing cells alongside a selective suppression of specific pro-inflammatory subpopulations over time. Thus, the therapeutic effect of ATGAM-based IST goes beyond 'simple' lymphodepletion.

To date, ATGAM is administered at a fixed dose per kilogram bodyweight, although its optimal dose remains unclear since its exposure-response profile has not been characterized in detail[2, 21, 22]. This study provides unique insight into ATGAM pharmacokinetics and offers important considerations regarding dosing. Consistent with data on rabbit-derived ATG[23, 24], we demonstrate that linear weight-based dosing causes variability in active ATGAM exposure between patients. In line with a previous report[25] that suggested a benefit of higher ATGAM exposures on relapse rates, we found that higher active ATGAM exposures tend to associate with increased neutrophil and reticulocyte counts starting 60 days post-ATGAM infusion. Although these associations did not reach statistical significance, the observed trend could be suggestive of a possible relationship between active ATGAM exposure and the timing of hematologic recovery. These findings may complement previous studies that identified patient- and disease-specific characteristics predicting response to IST, suggesting that hematologic recovery may be controlled by multiple factors[26-32]. The biological mechanism by which active ATGAM exposure may influence hematologic recovery remains unclear. In our study, active ATGAM exposure was not significantly associated with the extent or duration of T- or NK-cell depletion. Although we did not assess ciclosporin levels, their impact seems limited, given that ciclosporin dosing was concentration-controlled to a pre-specified target[2]. Interestingly, it has been reported that ATGAM can stimulate progenitor cells[33] and the release of factors regulating hematopoiesis[13, 34]. Thus, higher ATGAM exposures could have a favorable effect through a stronger influence on the progenitors in the bone marrow.

By applying flow cytometry, we provide a detailed description of both the short- and long-term immunological effects of ATGAM plus ciclosporin in AA patients. Although it is known that ATGAM results in less profound lymphodepletion compared to other ATG preparations[4], our findings show that immune reconstitution occurs early post-ATGAM while active ATGAM concentrations are still detectable. This indicates that a minimal level should be exceeded for adequate lymphodepletion, and that a better understanding of the exposure-response relationship of ATGAM is needed to optimize treatment across patients.

Importantly, our analyses revealed how successful IST may reshape the immune landscape to enable bone marrow recovery in AA patients. Our study therefore builds upon recent reports demonstrating the added value of high-dimensional single-cell techniques in deciphering the pathogenesis of AA[14, 15, 35, 36], and complements a comprehensive review of their application in AA[37]. Previously, using (imaging) mass cytometry on bone marrow samples from AA patients, we identified a disease-specific immune cell network of $CCR6^{++}$ B-cells, Th17-like[32, 38, 39] $CCR6^{+}$ memory $CD4^{+}$ T-cells and $KLRG1^{+}$ EMRA $CD8^{+}$ T-cells[14, 15]. These immune cells were significantly enriched in AA patients at diagnosis compared to healthy donors, and showed a trend towards normalization six months after successful IST, implying a pathogenic role. In this study, we extend these findings by confirming their increased presence at diagnosis. Importantly, we further show how these cells are reduced with IST through an analysis of unique series of PBMC samples collected pre- and up to 3.5 years post-ATGAM. Our study thereby provides a more dynamic visualization of the reshaping of the immune landscape compared to previous reports that generally focused on samples collected pre- and six months post-ATGAM[14, 15, 36, 39]. Although the analysis included only three patients, it allowed for a deeper investigation beyond the major immune lineages assessed in the full cohort of 44 AA patients, and sets the stage for more widely applied longitudinal analyses in future studies. We demonstrate that successful IST depletes potentially pathogenic populations via two distinct mechanisms: $KLRG1^{+}$ EMRA $CD8^{+}$ and $CCR6^{+}$ memory $CD4^{+}$ T-cells are depleted by ATGAM. In contrast, $CCR6^{++}$ B-cells and residual T-cells, including $CCR6^{+}$ memory $CD4^{+}$ T-cells, gradually decrease within several months during long-term ciclosporin use. These data indicate the persistence of potentially pathogenic immune cell subpopulations post-ATGAM, and could explain why long-term ciclosporin is needed to achieve durable response rates.

Based on prior studies[4, 13], we expected ATGAM to bind T-cells and to cause rapid but short-lived T-cell depletion. Our data confirm this effect and further reveal important differences among T-cell subpopulations. Specifically, memory T-cells were more profoundly depleted than naïve T-cells, suggesting that ATGAM targets cytotoxic T-cells, while preserving part of the antigen-naïve T-cell repertoire that provides protection against future pathogen encounters. This effect is more pronounced among $CD8^{+}$ T-cells compared to $CD4^{+}$ T-cells, and remains detectable up to six months post-ATGAM, likely due to the inhibition of T-cell

proliferation and differentiation by ciclosporin[40]. During this period, we observed reconstitution of CMV-specific $CD8^+$ T-cells, implying that ATGAM does not result in a full immune 'reset'. Although the recovery of pre-existing cells has been described with other ATG preparations[41], it raises questions on how successful IST eliminates potential autoreactive T-cells while preserving protective immune memory. We consider three possible explanations. First, ATGAM may exert a stronger effect on autoreactive T-cells compared to other memory T-cells, possibly due to differences in cellular state. Similarly, it is possible that, in the absence of infections, remaining autoreactive T-cells post-ATGAM may be more susceptible to ciclosporin compared to pathogenic-specific T-cells due to continued antigenic triggering. Finally, it could be that ATGAM depletes memory T-cells in the blood and bone marrow, while not affecting tissue-resident T-cells. This would suggest that autoreactive T-cells are limited to the blood and bone marrow, and that targeting these compartments alone could suffice to enable bone marrow recovery.

Since ATGAM has strong effects on T-cells, it is noteworthy that our data confirm that ATGAM does not have the same effect on B-cells[13]. Instead of depletion, we report a shift in the B-cell compartment, characterized by an increase of memory $CD27^+$ B-cells immediately post-ATGAM infusion, which gradually normalizes within one month. These $CD27^+$ B-cells comprised of a heterogeneous population of both non-switched and switched memory B-cells in a resting state. The $CD27^+$ B-cell population included pre-existing pathogen-specific cells as evidenced by the presence of tetanus toxoid-specific B-cells and was not proliferating. Therefore, we believe that the observed increase of $CD27^+$ B-cells may reflect redistribution of memory B-cells from the lymphoid organs into the circulation. This could be driven by an imbalance of chemotactic factors released following T-cell apoptosis. How B-cells survive ATGAM binding to their cell surface while T-cells are depleted should be clarified by future studies. Our data revealed no increased resistance of B-cells to complement-mediated lysis, nor an influence of Fc-binding. Given that ATGAM is a polyclonal antibody preparation generated against thymocytes, it is possible that ATGAM induces T-cell apoptosis by triggering T-cell activation (e.g. via anti-CD3 or TCR binding), without activating apoptotic pathways in B-cells.

To conclude, we unveil active ATGAM exposure as a clinically relevant factor influencing hematologic recovery in AA. We further demonstrate that successful IST with ATGAM plus long-term ciclosporin exerts differential effects among major lymphoid lineages, leading to selective depletion and suppression of $CCR6^+$ and $KLRG1^+$ T- and B-cell subpopulations implicated in AA pathogenesis. These findings confirm their potential pathogenicity, and establish these subpopulations as promising targets for targeted treatment.

References

1. Young NS. Aplastic Anemia. N Engl J Med. 2018;379(17):1643-1656.
2. Kulasekararaj A, Cavenagh J, Dokal I, et al. Guidelines for the diagnosis and management of adult aplastic anaemia: A British Society for Haematology Guideline. Br J Haematol. 2024;204(3):784-804.
3. Halkes CJ, Veelken H, Falkenburg JH. Horse versus rabbit antithymocyte globulin in aplastic anemia. N Engl J Med. 2011;365(19):1842-1843.
4. Scheinberg P, Nunez O, Weinstein B, et al. Horse versus rabbit antithymocyte globulin in acquired aplastic anemia. N Engl J Med. 2011;365(5):430-438.
5. Peffault de Latour R, Kulasekararaj A, Iacobelli S, et al. Eltrombopag Added to Immunosuppression in Severe Aplastic Anemia. N Engl J Med. 2022;386(1):11-23.
6. Genestier L, Fournel S, Flacher M, Assossou O, Revillard JP, Bonnefoy-Berard N. Induction of Fas (Apo-1, CD95)-mediated apoptosis of activated lymphocytes by polyclonal antithymocyte globulins. Blood. 1998;91(7):2360-2368.
7. Mohty M. Mechanisms of action of antithymocyte globulin: T-cell depletion and beyond. Leukemia. 2007;21(7):1387-1394.
8. Elliott JF, Lin Y, Mizel SB, Bleackley RC, Harnish DG, Paetkau V. Induction of interleukin 2 messenger RNA inhibited by cyclosporin A. Science. 1984;226(4681):1439-1441.
9. Heidt S, Roelen DL, Eijsink C, et al. Calcineurin inhibitors affect B cell antibody responses indirectly by interfering with T cell help. Clin Exp Immunol. 2010;159(2):199-207.
10. Popow I, Leitner J, Grabmeier-Pfistershammer K, et al. A comprehensive and quantitative analysis of the major specificities in rabbit antithymocyte globulin preparations. Am J Transplant. 2013;13(12):3103-3113.
11. Bourdage JS, Hamlin DM. Comparative polyclonal antithymocyte globulin and antilymphocyte/antilymphoblast globulin anti-CD antigen analysis by flow cytometry. Transplantation. 1995;59(8):1194-1200.
12. Raefsky EL, Gascon P, Gratwohl A, Speck B, Young NS. Biological and immunological characterization of ATG and ALG. Blood. 1986;68(3):712-719.
13. Feng X, Scheinberg P, Biancotto A, et al. In vivo effects of horse and rabbit antithymocyte globulin in patients with severe aplastic anemia. Haematologica. 2014;99(9):1433-1440.
14. Pool ES, Kooy-Winkelaar Y, van Unen V, et al. Mass cytometric analysis unveils a disease-specific immune cell network in the bone marrow in acquired aplastic anemia. Front Immunol. 2023;14:1274116.
15. Pool ES, Luk SJ, Ijsselsteijn ME, et al. Imaging mass cytometry reveals the order of events in the pathogenesis of immune-mediated aplastic anemia. Blood. 2025;146(8):951-963.
16. Tjon JM-L, Hussen-Dassen LGMv, Nur E, et al. Dutch guidelines for diagnostics and treatment of acquired aplastic anemia in adults. Nederlands Tijdschrift voor Hematologie. 2024;
17. Rebello P, Hale G. Pharmacokinetics of CAMPATH-1H: assay development and validation. J Immunol Methods. 2002;260(1-2):285-302.
18. Van Gassen S, Callebaut B, Van Helden MJ, et al. FlowSOM: Using self-organizing maps for visualization and interpretation of cytometry data. Cytometry A. 2015;87(7):636-645.
19. Comets E, Lavenu A, Lavielle M. Parameter Estimation in Nonlinear Mixed Effect Models Using saemix, an R Implementation of the SAEM Algorithm. J Stat Softw. 2017;80(3):1-41.
20. Pfizer. ATGAM (anti-thymocyte globulin (equine) sterile solution) Perscribing Information. Available from: https://labeling.pfizer.com/ShowLabeling.aspx?id=12213 [accessed on 8 January 2025]
21. Scott A, Morris K, Butler J, Mills AK, Kennedy GA. Treatment of aplastic anaemia with lower-dose anti-thymocyte globulin produces similar response rates and survival as per standard dose anti-thymocyte globulin schedules. Intern Med J. 2016;46(10):1198-1203.
22. Young N, Griffith P, Brittain E, et al. A multicenter trial of antithymocyte globulin in aplastic anemia and related diseases. Blood. 1988;72(6):1861-1869.
23. Admiraal R, van Kesteren C, Jol-van der Zijde CM, et al. Population pharmacokinetic modeling of Thymoglobulin((R)) in children receiving allogeneic-hematopoietic cell transplantation: towards improved survival through individualized dosing. Clin Pharmacokinet. 2015;54(4):435-446.
24. Oostenbrink LVE, Von Asmuth EGJ, Jol-van der Zijde CM, et al. Anti-T-lymphocyte globulin exposure is associated with acute graft-versus-host disease and relapse in pediatric acute lymphoblastic leukemia patients undergoing hematopoietic stem cell transplantation: a multinational prospective study. Haematologica. 2024;109(9):2854-2863.

25. Walter J, Rolles B, Schumacher Y, et al. Analysis of the Impact of Body Mass Index (BMI) on the Durability of Response in Patients with Aplastic Anemia Treated with Weight-Adjusted Horse Anti-Thymocyte Globulin (hATG). Blood. 2023;142(Supplement 1):5641.
26. Scheinberg P, Wu CO, Nunez O, Young NS. Predicting response to immunosuppressive therapy and survival in severe aplastic anaemia. Br J Haematol. 2009;144(2):206-216.
27. Yoshizato T, Dumitriu B, Hosokawa K, et al. Somatic Mutations and Clonal Hematopoiesis in Aplastic Anemia. N Engl J Med. 2015;373(1):35-47.
28. Narita A, Muramatsu H, Sekiya Y, et al. Paroxysmal nocturnal hemoglobinuria and telomere length predicts response to immunosuppressive therapy in pediatric aplastic anemia. Haematologica. 2015;100(12):1546-1552.
29. Zhao X, Zhang L, Jing L, et al. The role of paroxysmal nocturnal hemoglobinuria clones in response to immunosuppressive therapy of patients with severe aplastic anemia. Ann Hematol. 2015;94(7):1105-1110.
30. Sugimori C, Chuhjo T, Feng X, et al. Minor population of CD55-CD59- blood cells predicts response to immunosuppressive therapy and prognosis in patients with aplastic anemia. Blood. 2006;107(4):1308-1314.
31. Zaimoku Y, Patel BA, Kajigaya S, et al. Deficit of circulating CD19(+) CD24(hi) CD38(hi) regulatory B cells in severe aplastic anaemia. Br J Haematol. 2020;190(4):610-617.
32. Kordasti S, Costantini B, Seidl T, et al. Deep phenotyping of Tregs identifies an immune signature for idiopathic aplastic anemia and predicts response to treatment. Blood. 2016;128(9):1193-1205.
33. Huang AT, Mold NG, Zhang SF. Antithymocyte globulin stimulates human hematopoietic progenitor cells. Proc Natl Acad Sci U S A. 1987;84(16):5942-5946.
34. Nimer SD, Golde DW, Kwan K, Lee K, Clark S, Champlin R. In vitro production of granulocyte-macrophage colony-stimulating factor in aplastic anemia: possible mechanisms of action of antithymocyte globulin. Blood. 1991;78(1):163-168.
35. Lundgren S, Huuhtanen J, Keranen M, et al. Single-cell analysis of aplastic anemia reveals a convergence of NK and NK-like CD8(+) T cells with a disease-associated TCR signature. Sci Transl Med. 2025;17(787):eadl6758.
36. Wu Z, Gao S, Feng X, et al. Human autoimmunity at single cell resolution in aplastic anemia before and after effective immunotherapy. Nat Commun. 2025;16(1):5048.
37. Wu Z, Young NS. Single-cell genomics in acquired bone marrow failure syndromes. Blood. 2023;142(14):1193-1207.
38. de Latour RP, Visconte V, Takaku T, et al. Th17 immune responses contribute to the pathophysiology of aplastic anemia. Blood. 2010;116(20):4175-4184.
39. Kordasti S, Marsh J, Al-Khan S, et al. Functional characterization of CD4+ T cells in aplastic anemia. Blood. 2012;119(9):2033-2043.
40. Jenkins MK, Schwartz RH, Pardoll DM. Effects of cyclosporine A on T cell development and clonal deletion. Science. 1988;241(4873):1655-1658.
41. Havenith SH, Remmerswaal EB, Bemelman FJ, et al. Rapid T cell repopulation after rabbit anti-thymocyte globulin (rATG) treatment is driven mainly by cytomegalovirus. Clin Exp Immunol. 2012;169(3):292-301.

Tables

Table 1. Patient characteristics.	
Characteristic	**Patients (n=44)**
Age at diagnosis (median, range in years)	54 (20-79)
Sex (n)	
Male	26
Female	18
Weight at diagnosis (median, range in kg)	80 (51-120)
Body mass index at diagnosis (median, range)	24.7 (17.6-34.3)
Height at diagnosis (median, range in cm)	176 (156-198)
Severity of disease at diagnosis (n)	
Non-severe AA	7
Severe AA	23
Very severe AA	14
Total lymphocyte count pre-ATGAM ($\cdot 10^6$/L)*#	1375 (260-2890)
$CD4^+$ T-cell count pre-ATGAM ($\cdot 10^6$/L)*#	732 (21-1479)
$CD8^+$ T-cell count pre-ATGAM ($\cdot 10^6$/L)*#	363 (71-949)
NK-cell count pre-ATGAM ($\cdot 10^6$/L)*#	77 (4-291)
B-cell count pre-ATGAM ($\cdot 10^6$/L)*	124 (17-631)
Response to IST 6 months post-ATGAM (n)	
Non-response	21
Partial response	14
Complete response	5
Unknown (died <6 months after first ATGAM infusion)	4
**Cell counts between days -2 to 0 pre-ATGAM infusion; #Data missing for 2 patients.*	

Main figure legends

Figure 1. Active ATGAM binding specificities and concentration-time profiles in plasma from AA patients. [A] Experimental approach. Donor PBMCs were incubated with plasma samples collected pre- and post-ATGAM, stained and analyzed by flow cytometry to determine the plasma levels of free active ATGAM capable of binding to human lymphocyte lineages. **[B]** Measured active ATGAM levels in patient plasma (in arbitrary units/mL; n=44 patients) in time before, during and after ATGAM infusion on days 0-4. **[C]** Flow cytometric plots demonstrating the binding of active ATGAM in plasma from a representative patient (UPN33) to $CD4^+$ T-cells, $CD8^+$ T-cells, NK-cells or B-cells from a healthy donor, measured using an Alexa Fluor 488-conjugated anti-horse IgG antibody. **[D]** Model-estimated active ATGAM plasma concentrations over time before, during and after ATGAM infusion on days 0-4. Mean active ATGAM concentrations are presented for patients within the lowest (blue), medium (yellow) and highest (red) body weight quantiles, who received 4 consecutive days 40mg/kg/day ATGAM. Insert: Correlation between model-estimated active ATGAM exposure and body weight. **[E-F]** Covariate plots showing the relationship between body weight and the inter-individual variability in estimated active ATGAM clearance (E) or volume of distribution (F). Each dot represents one patient. Each dot represents one patient. Only patients that received the standard dosing regimen of 4 consecutive days 40mg/kg/day ATGAM are shown.

Figure 2. Impact of active ATGAM exposure on peripheral blood counts. [A] Histogram showing the distribution of active ATGAM exposure across the patient cohort. **[B-C]** Absolute neutrophil (B) and reticulocyte (C) counts over time up to 180 days after ATGAM infusion on days 0-4. Light gray lines present individual patients. Blue, yellow and red lines present group medians of low, medium and high active ATGAM exposure groups, on days 0, 30, 60, 91, 122, 152 and 180 +/- 7 days, respectively. Cell counts were unavailable for 2 (day 30), 5 (day 60), 9 (day 91), 9 (day 122), 7 (day 152) and 9 (day 180) patients divided across all exposure groups. Box plots represent the group median, whiskers represent 1.5 * interquartile range. **[D]** Median model-estimated active ATGAM concentrations capable of binding to all lymphocytes, $CD4^+$ T-cells, $CD8^+$ T-cells, NK-cells or B-cell plotted against absolute total lymphocyte, $CD4^+$ T-cell, $CD8^+$ T-cell, NK-cell or B-cell counts, respectively. Light gray lines present cell counts of individual patients. Blue, yellow and red lines present median cell counts of low, medium and high active ATGAM exposure groups, respectively. Model-estimated lymphocyte, $CD4^+$ T-cell, $CD8^+$ T-cell, NK-cell counts are presented, whereas observed B-cell counts are shown.

Figure 3. Binding of ATGAM and the impact of ATGAM-based IST on lymphocytes from AA patients. [A] $3 \cdot 10^6$ single, live lymphocytes downsampled from all PBMC samples (UPN13, UPN15, UPN31 and five controls) visualized using an UMAP analysis. Colors indicate major lymphoid lineages or marker expression values. **[B]** UMAP plots showing the cellular composition of the lymphoid compartment in peripheral blood from UPN31 before and over time following ATGAM infusion on days 0-4. The signal of the Alexa Fluor 488-conjugated anti-horse IgG antibody is shown. $0.1 \cdot 10^6$ single, live lymphocytes are shown per time point. **[C]** Frequencies of major lymphoid lineages, shown as a percentage of all single, live lymphocytes per time point. Each line represents an individual patient. **[D]** Flow cytometry plots visualizing the presence of ATGAM directly bound to T-, NK- or B-cells from UPN31 over

time, detected using an Alexa Fluor 488-conjugated anti-horse IgG antibody incorporated into the spectral flow cytometry panel.

Figure 4. Impact of ATGAM-based IST at the immune subpopulation level in a representative AA patient. [A-C] Flow cytometry plots visualizing the composition of the [A] $CD4^+$ T-cell compartment, [B] $CD8^+$ T-cell compartment and [C] B-cell compartment from patient UPN31 before and over time following start of ATGAM-based IST on day 0. CM: central memory, EM: effector memory, EMRA: terminally differentiated effector memory.

Figure 5. Dynamics of memory T-cells and $CD27^+$ B-cells, and identity of $CD27^+$ B-cells, post-ATGAM. [A-C] Frequencies of memory $CD4^+$ T-cells, memory $CD8^+$ T-cells or $CD27^+$ B-cells over time, quantified in all three AA patients and controls. Memory T-cells include central memory, effector memory and terminally differentiated effector memory T-cells. **[D]** Isotype distribution of the $CD27^+$ B-cells from UPN31 on day 13 after the first ATGAM infusion, and the mean of two age-matched controls. **[E**] Expression of CD21, CD24, CD80, CD86 and CD95 on $CD27^+$ B-cells from patient UPN31 on day 13, and the mean of two age-matched controls. Median fluorescence intensities are shown. **[F]** Expression of complement inhibitors CD46 and CD55 on $CD27^+$ B-cells from patient UPN31 on day 13, and the mean of two age-matched heathy controls. Median fluorescence intensities are shown. **[G]** Flow cytometry plots showing the presence of tetanus toxoid-specific $CD27^+$ B-cells in patient UPN31 on day 13, and an age-matched healthy control. $0.1 \cdot 10^6$ $CD27^+$ B-cells are shown per plot.

Figure 6. Effects of ATGAM on pre-existing and potentially pathogenic subpopulations. [A] Flow cytometry plots showing the presence of CMV-specific $CD8^+$ T-cells within the $CD8^+$ T-cell compartment at diagnosis and after the first ATGAM infusion in patient UPN31. **[B]** Frequencies of CMV-specific $CD8^+$ T-cells, quantified as a frequency of all $CD8^+$ T-cells in patients UPN15 and UPN31, and all controls. **[C-D]** Histograms showing CCR6 expression on all $CD19^+$ B-cells (C) or $CCR6^+$ memory $CD4^+$ T-cells (D) in the three AA patients over time following ATGAM infusion and ciclosporin treatment. **[E-H]** Frequencies of all $KLRG1^+$ EMRA $CD8^+$ T-cells, CMV-specific $KLRG1^+$ EMRA $CD8^+$ T-cells, Granzyme B^+ cytotoxic T-cells and $CD38^+$ activated T-cells in all three AA patients over time following ATGAM infusion.

Figure 1

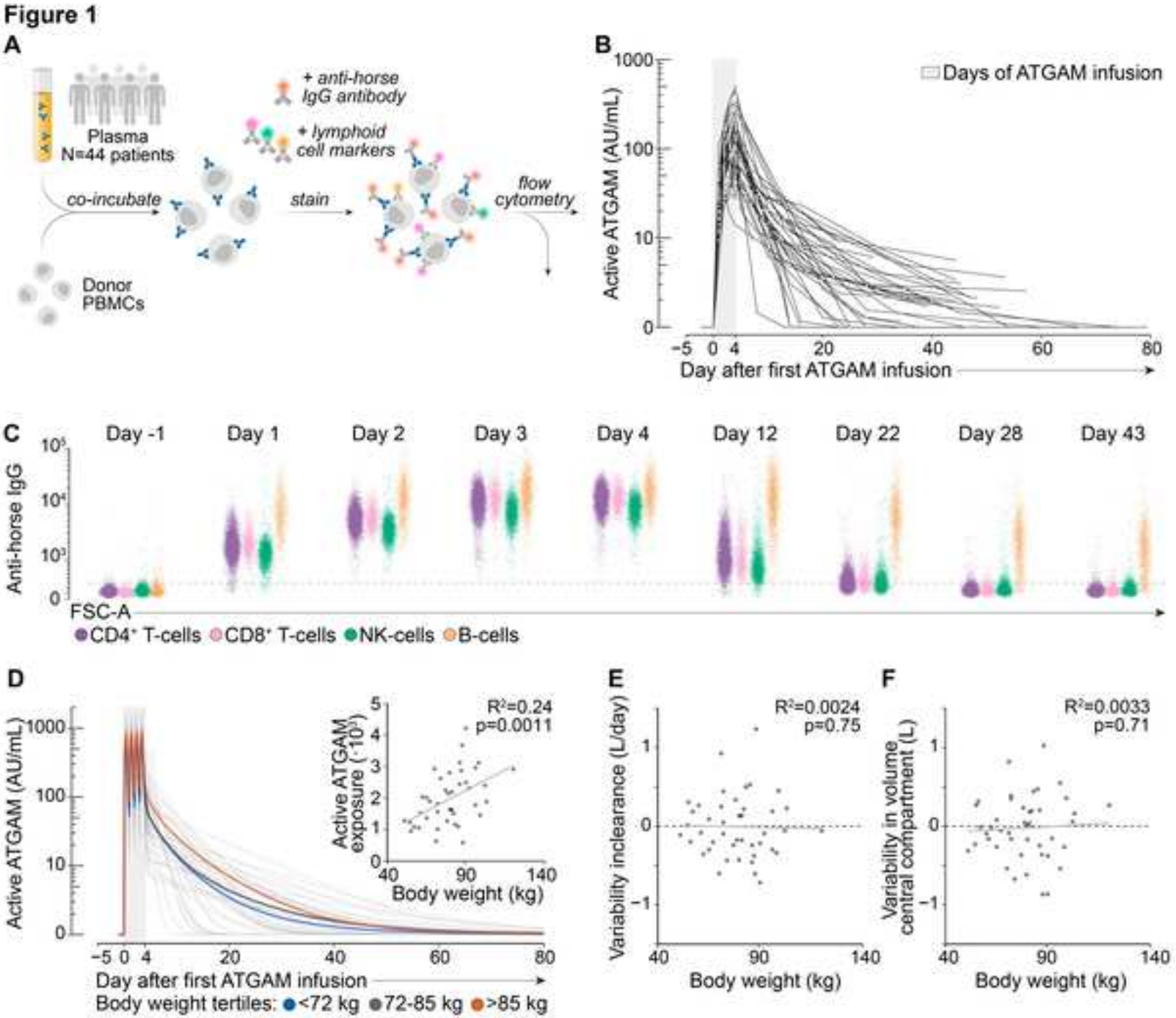

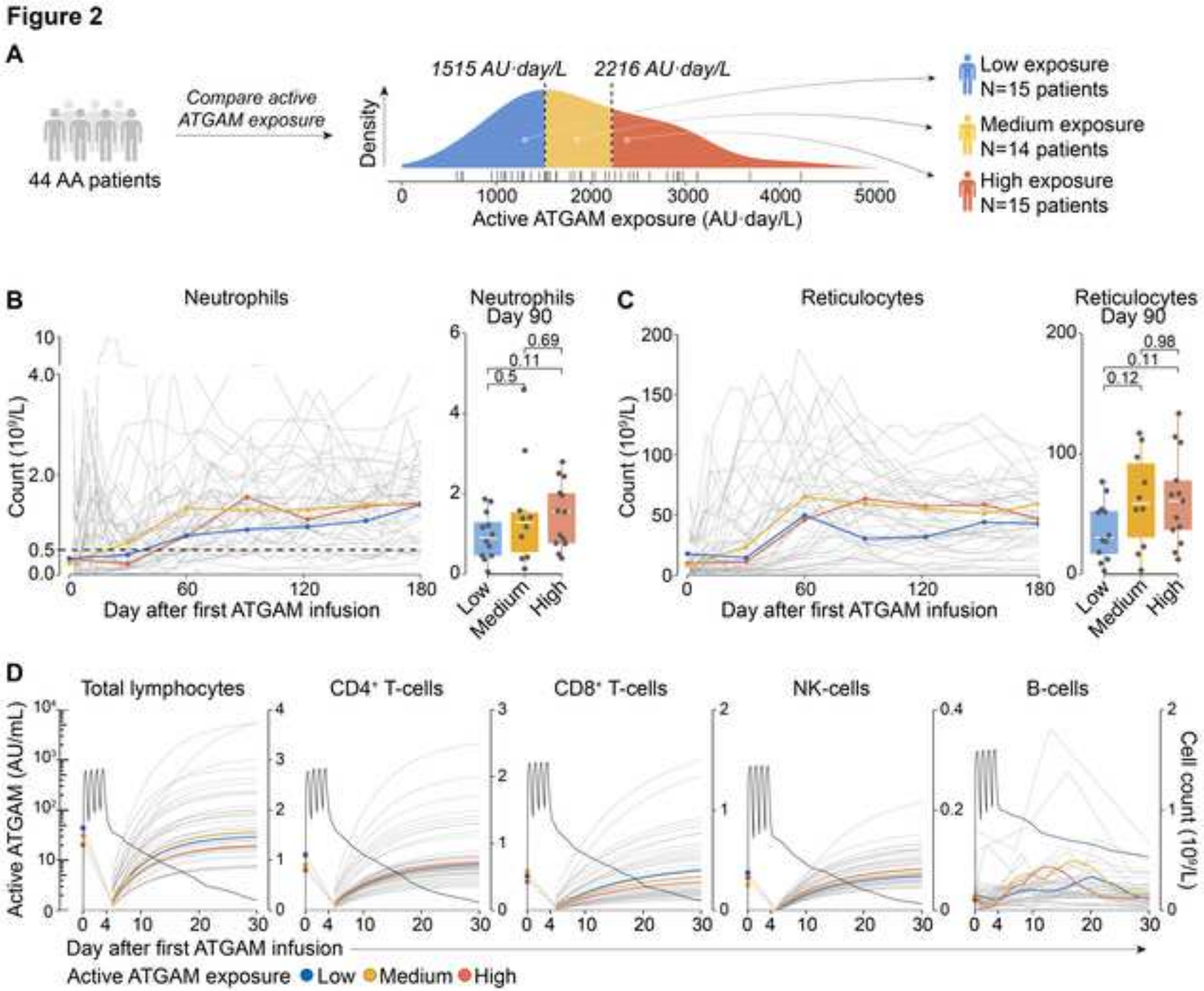

Figure 3

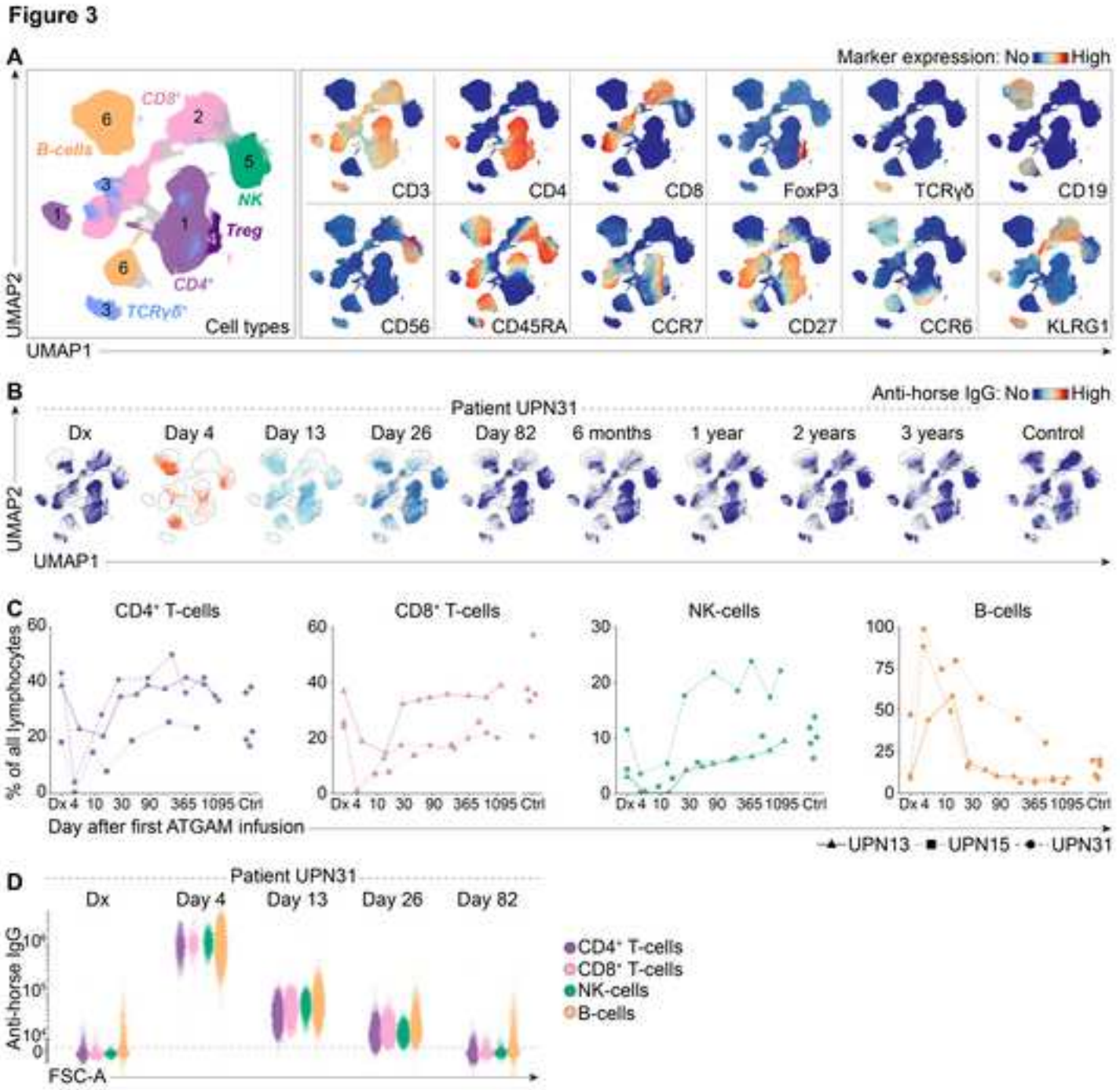

Figure 4

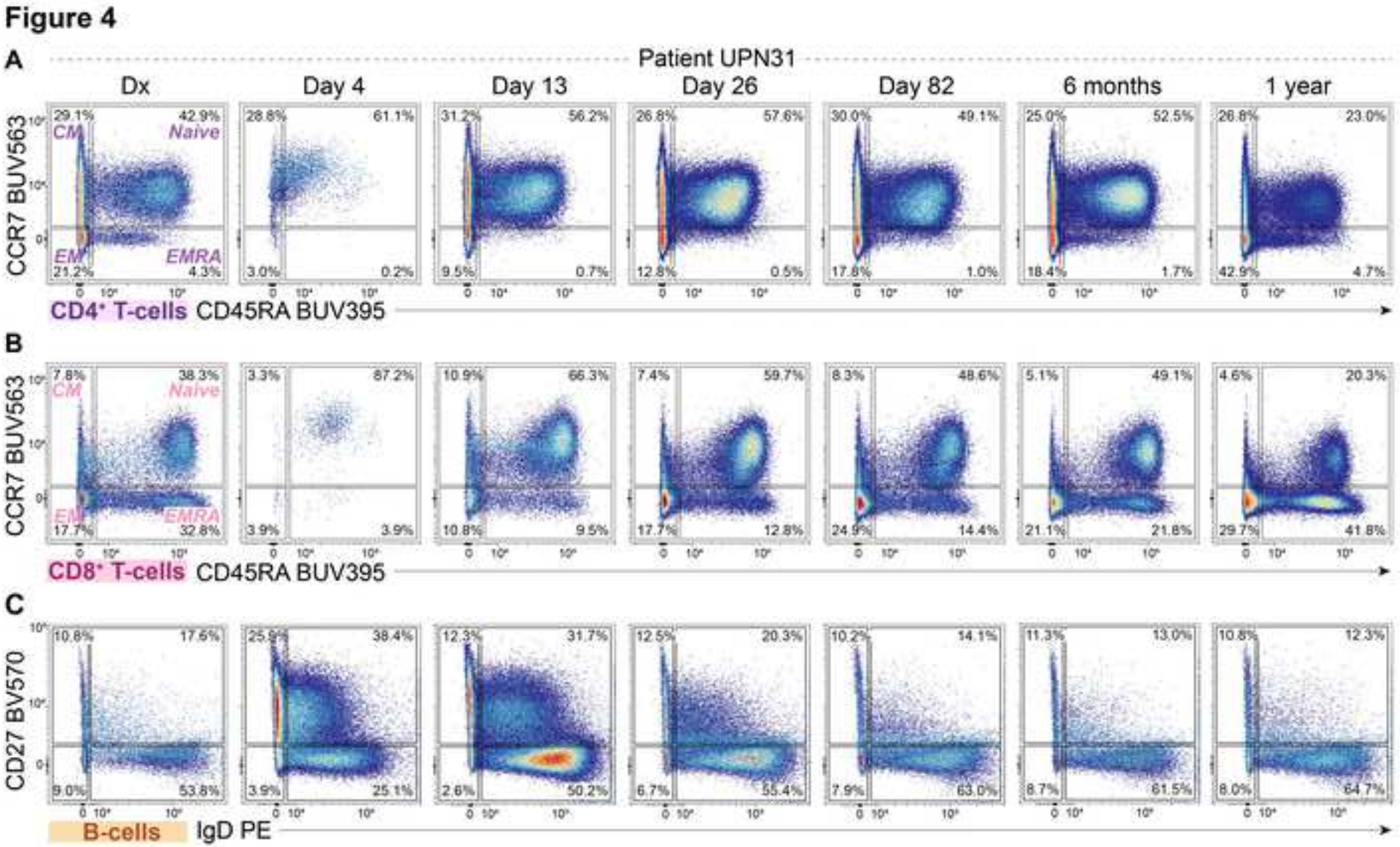

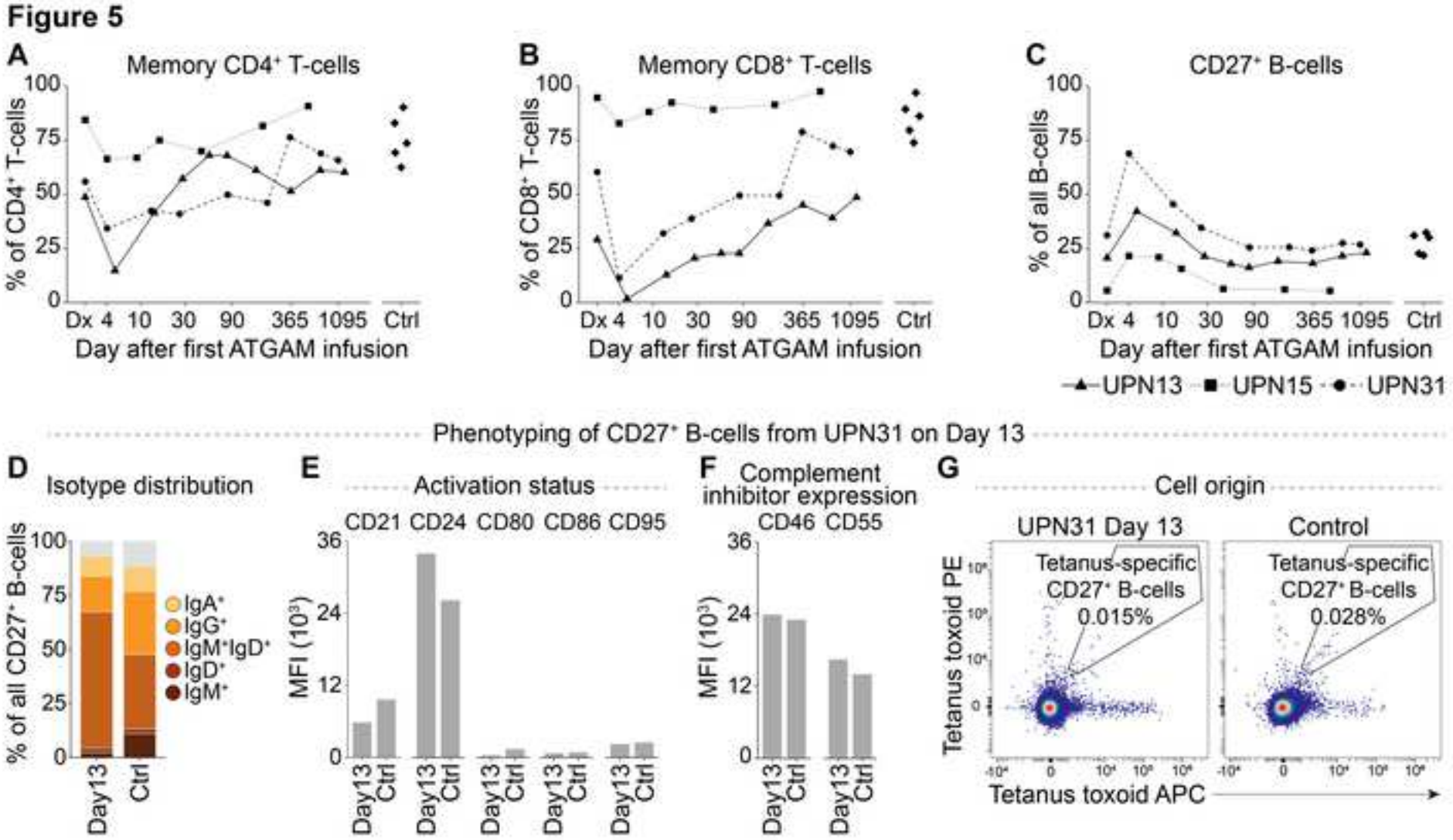

Figure 6

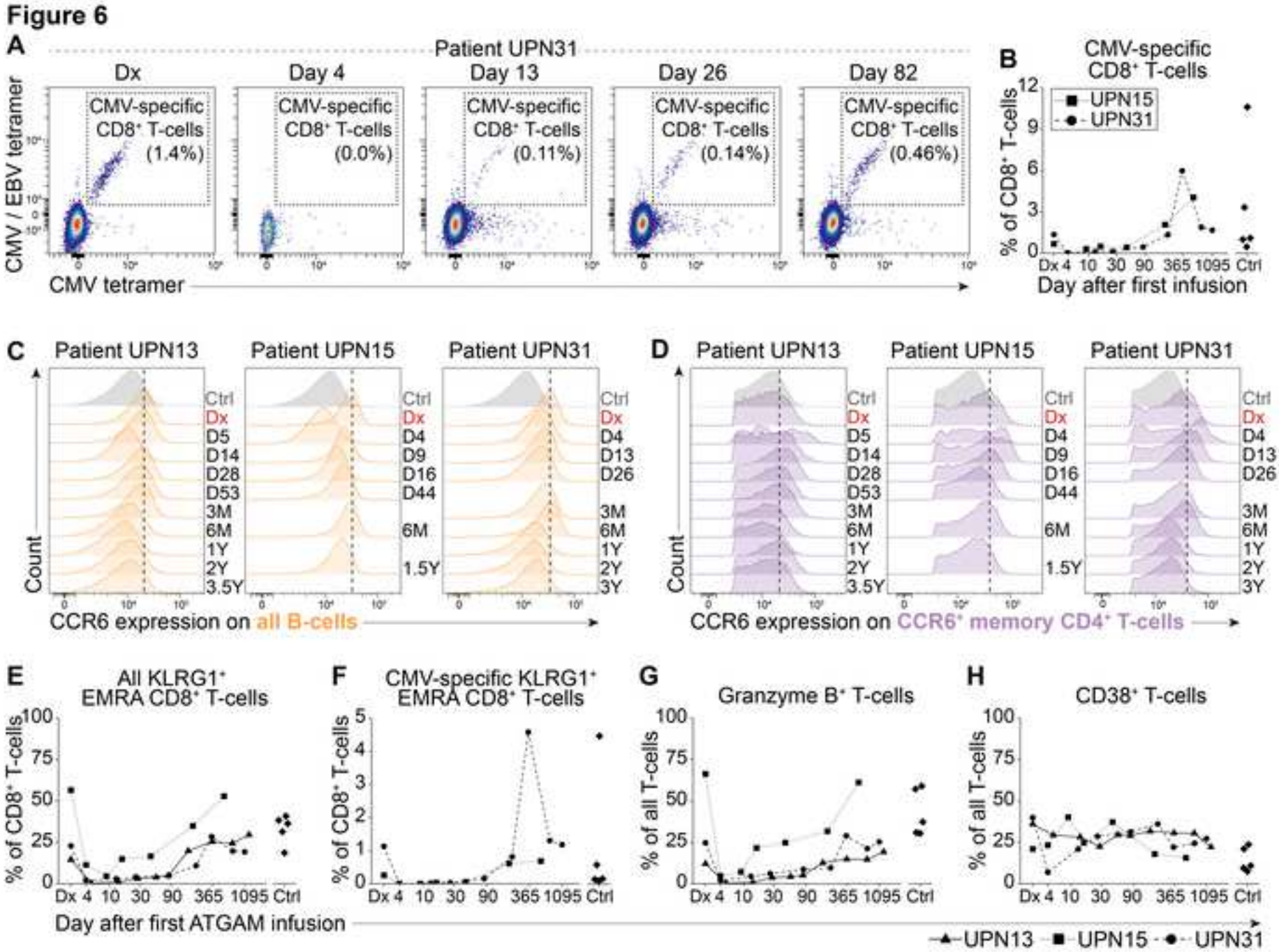

Supplementary data

Selective lymphodepletion underlies the efficacy of horse anti-thymocyte globulin-based immunosuppressive therapy in aplastic anemia

Emma S. Pool[1], Cilia R. Pothast[1], Shannah Gennesse[1], Esther H.M. van Egmond[1], Julia M. Giezen[2], Sabrina A.J. Veld[1], René E.M. Toes[2], Frits Koning[3], Constantijn J.M. Halkes[1], Mirjam H.M. Heemskerk[1], Dirk Jan A.R. Moes[4] and Jennifer M-L. Tjon[1]

[1] Department of Hematology, Leiden University Medical Center, Leiden, The Netherlands
[2] Department of Rheumatology, Leiden University Medical Center, Leiden, The Netherlands
[3] Department of Immunology, Leiden University Medical Center, Leiden, The Netherlands
[4] Department of Clinical Pharmacy and Toxicology, Leiden University Medical Center, Leiden, The Netherlands

Supplementary methods

Quantification of total ATGAM concentrations

Total ATGAM was defined as all horse IgG antibodies in the ATGAM preparation[1]. Total ATGAM concentrations in patient plasma were quantified by sandwich ELISA. 96-well plates were coated overnight at 4°C with goat anti-horse IgG antibodies at a dilution of 1:2500 in PBS (Jackson Immunoresearch, cat 108-005-003). Next, plates were blocked, washed using PBS with 0.005% Tween20, and incubated with diluted patient plasma samples for two hours at room temperature. Each sample was analyzed across eight serial dilutions. Subsequently, plates were washed five times using PBS with 0.005% Tween20 and incubated with a peroxidase-conjugated secondary goat anti-horse antibody at a dilution of 1:25,000. After a one hour incubation at room temperature, plates were washed five times using PBS with 0.005% Tween20 and stained with TMB substrate buffer for five minutes in the dark. Finally, staining was stopped and plates were measured at 450nm on a microplate photometer (ThermoFisher Multiskan FC). Total ATGAM concentrations in µg/mL in each plasma sample were calculated using the linear range of a standard curve, which was created by including serial dilutions of known ATGAM concentrations in each experiment.

Quantification of active ATGAM concentrations

Active ATGAM was defined as the fraction of ATGAM that is capable of binding to human lymphocytes. To quantify active ATGAM concentrations in plasma, flow cytometry was performed based on a validated protocol for the quantification of alemtuzumab levels in patient plasma[2], which since has been optimized for the measurement of rabbit-derived anti-thymocyte globulin plasma concentrations[3]. Recent work shows this assay resulted in high-quality pharmacokinetic data for a cohort of 121 acute lymphoblastic leukemia patients who received rabbit-derived anti-thymocyte globulin as part of the conditioning regimen pre-HSCT[4]. In our study, first, cryopreserved PBMCs isolated from a healthy donor were thawed and plated in 96-well plates. PBMCs from the same donor were used in all experiments to enable comparisons between experiments. Subsequently, cells were incubated with non-diluted and 3x, 9x, and 27x diluted patient plasma for 30 minutes at 4°C. Afterwards, cells were washed twice in PBS and incubated with an AlexaFluor 488-conjugated goat anti-horse antibody diluted at 1:100 in a volume of 10µL for 30 minutes at 4°C (Jackson Immunoresearch, cat 108-545-003). Next, cells were washed twice in PBS and stained with a panel of six fluorochrome-conjugated antibodies in a volume of 10µL to distinguish all major immune lineages. The following antibodies were used: APC-H7 anti-human CD3 antibody diluted at 1:60 (BD Biosciences, cat 641406); PE-Cy7 anti-human CD4 antibody diluted at 1:3000 (Beckman Coulter, cat 6607101); Pacific Blue anti-human CD8 antibody diluted at 1:2000 (BioLegend, cat 301026); PerCP anti-human CD14 antibody diluted at 1:50 (BD Biosciences, cat 563372); APC anti-human CD19 antibody diluted at 1:50 (BD Biosciences, cat 555415) and BV510 anti-human CD56 antibody at 1:50 (BD Biosciences, cat 563041). After a 30 minute incubation at 4°C, cells were washed and measured immediately on the BD LSRFortessa™ cell analyzer (BD Biosciences). Data were analyzed in FlowJo (BD Biosciences) or OMIQ (Dotmatics). The gating strategy presented **Figure S1** determined the geometric mean fluorescence intensity of AlexaFluor 488-stained total lymphocytes, $CD4^+$ T-cells, $CD8^+$ T-cells, B-cells, NK-cells and monocytes in each acquired sample. Concentrations of ATGAM capable of binding to all

lymphocytes (active ATGAM), $CD4^+$ T-cells ($CD4^+$ T-cell-binding active ATGAM), $CD8^+$ T-cells ($CD8^+$ T-cell-binding active ATGAM), $CD19^+$ B-cells (B-cell-binding active ATGAM) and $CD56^+$ NK-cells (NK-cell-binding active ATGAM) were then calculated using the mean of two reference curves, which were created by exposing the PBMCs to known concentrations of ATGAM in each experiment. To ensure consistency between experiments, the reference curves were aliquoted and stored at -20°C to enable their use across experiments. Active ATGAM concentrations were calculated in arbitrary units (AU), and the concentration of 1mg/mL ATGAM was arbitrarily set as 1000 AU/mL. The lower limit of quantification (LLoQ) of the assay was 0.02 AU/mL. At high ATGAM concentrations of >200 AU/mL in patient plasma, accurate gating of NK-cells could not be performed. As a result, concentrations of NK-cell-binding active ATGAM were not determined on days 3 and/or 4 after the first ATGAM dose for a few patients. To confirm the robustness of the assay, we analyzed the duplicate measurement of undiluted patient plasma included in each experiment, and evaluated duplicate measurements of serial dilutions of ATGAM. This revealed strong correlations between technical duplicates ($p<0.001$), underscoring within-experiment reproducibility (**Figure S2A**). To confirm reproducibility between experiments, plasma samples collected from several AA patients pre- and post-ATGAM were measured in duplicate in independent experiments, which resulted in highly comparable results (**Figure S2B**).

Population pharmacokinetic modelling and estimation of ATGAM exposure

To estimate the full concentration *versus* time profile of total and active ATGAM, non-linear mixed-effects modeling was performed using the acquired total or active ATGAM concentration-time data. Model development was performed in NONMEM version 7.4.4 (Icon Development Solutions, Ellicott City, MD). Pirana version 2.9.8 (Certara, Princeton, NJ) was used as a modeling platform, while R version 4.4.1 ran in RStudio version 2023.03 was used for data visualization. Pharmacokinetic parameters were estimated using a first-order conditional estimation with interaction approach (FOCE+I). To identify the model with the best fit for the concentration-time data, both one- and two-compartment models, incorporating linear, non-linear or parallel linear and non-linear elimination, were evaluated. Inter-individual variability (IIV) in parameter estimates was evaluated using an exponential error model, while residual unexplained variability was characterized by testing additive, proportional and combined error models. Inter-occasion variability was examined for all pharmacokinetic parameters to determine whether pharmacokinetics varied between different ATGAM infusions. A detailed overview of the steps taken during model development is shown in **Tables S2** and **S3**.

To find the model that best described the concentration-time data, we compared each candidate model using the objective function value (OFV; -2 log likelihood). A lower OFV indicated a better fit, and a model was considered to have a significantly improved fit if its OFV decreased by at least 6.63 ($p\leq0.01$; based on 1 degree of freedom, and assuming a chi-square distribution). Models were also assessed visually using goodness-of-fit (GOF) plots. These plots compared observed (measured) ATGAM concentrations against both individual predicted (IPRED) and population predicted (PRED) ATGAM concentrations to assess how well the model captured the measured concentration-time data. Other GOF plots compared conditional weighted residuals (CWRES) against time or PRED. The aim of these plots was

to identify any systematic differences between the predicted and observed (measured) ATGAM concentrations. Other considerations in model selection included model pharmacokinetic parameter stability, inter-individual variability (IIV) and shrinkage, to ensure the model was well structured and not too complex for the available data.

To better understand the differences in the concentration-time profile of ATGAM between patients and to improve the predictive power of the model, we studied the influence of clinical covariates on the population pharmacokinetics of ATGAM. Potential covariates were selected based on physiological plausibility, and included age, sex and body weight. The effect of the selected covariates on ATGAM pharmacokinetics was initially evaluated visually, by examining how clearance (CL) or volume of distribution (V) were influenced by these covariates across all patients. Eta CL and V *versus* covariate plots were used. Given that ATGAM includes antibodies that can bind lymphocytes, we also assessed whether CL or V were influenced by differences in lymphocyte count pre-ATGAM between patients.

The final population pharmacokinetic models for total or active ATGAM were validated using prediction-corrected visual predictive checks (pcVPC)[5]. This approach relied on running the model 500 times to simulate new datasets, which were then compared to the observed (measured) ATGAM concentrations to confirm the performance of the model in predicting the ATGAM concentrations between patients. In addition, non-parametric bootstraps with 1000 simulations were performed to evaluate the precision of the final parameter estimates.

To estimate the full concentration *versus* time curve of the active ATGAM fractions capable of binding to $CD4^+$ T-cells, $CD8^+$ T-cells, B cells or NK cells, we ran the final population pharmacokinetic model (posthoc estimation) for active ATGAM using the concentration *versus* time data of each of these active ATGAM fractions.

To enable correlation analyses between ATGAM exposure and clinical parameters, we used the final population pharmacokinetic models that best described the concentration *versus* time data for total or active ATGAM to estimate individual pharmacokinetic parameters. These estimates were then used to calculate patients' cumulative exposure to total or active ATGAM, which was defined as the area under the concentration *versus* time curve ($AUC_{0\text{-}inf}$).

Immune reconstitution data

To correct for missing immune reconstitution data, we performed non-linear mixed effect modeling using the SAEMIX package[6] in R version 4.4.1. We used exponential models to predict total lymphocyte, $CD4^+$ T-cell, $CD8^+$ T-cell and NK-cell counts on each day between days 4 and 40 after start of ATGAM infusion in each patient. These models considered both the general trend across all patients and inter-individual differences. Predictions were only made for patients who had at least one measurement available between days 4 and 40 following infusion (n=43 patients), and are presented in **Figure S5**. B-cell reconstitution was not modeled using SAEMIX since no consistent trends were observed in the B-cell count-time data shortly after ATGAM administration between patients.

Spectral flow cytometry data acquisition and analysis

For deep immunophenotyping both before and at various time points after start of IST, spectral flow cytometry was performed. A 25-marker panel was designed to immunophenotype all major lymphoid lineages and to examine the binding of ATGAM to in-depth phenotyped immune cell subpopulations (**Table S1**). Cryopreserved PBMC samples from 3 AA patients, collected at AA diagnosis and up to 3.5 years after ATGAM infusion were studied (patients UPN13, UPN15 and UPN31; 7-10 samples per patient). All patients had very severe AA (VSAA), received four consecutive days 40 mg/kg/day ATGAM, responded to IST and were CMV seropositive at time of AA diagnosis. As a reference, cryopreserved PBMC samples from 5 age-, sex- and CMV status-matched healthy donors were studied. PBMC samples were thawed, plated into 96-well plates and rested at 37°C overnight. The next morning, cells were stained for viability with Zombie-NIR. Subsequently, cells were washed and stained with AlexaFluor 488-conjugated goat anti-horse IgG (Jackson Immunoresearch) diluted at 1:100 in a volume of 10µL for 30 minutes at room temperature to detect ATGAM-bound cells. Next, cells were washed and stained for 7 of 25 markers of the panel extracellularly in a volume of 10µL. This included BUV615-, PE- or APC-conjugated peptide-HLA tetramers, which were produced in-house and were added to evaluate the presence of CMV- and EBV-specific $CD8^+$ T-cells over time. After a 30 minute incubation at room temperature, cells were washed, fixed and stained intracellularly for the remaining 17 markers of the flow cytometry panel using the FoxP3/Transcription Factor Staining Buffer Set (Invitrogen; cat 00-5523-00) according to the manufacturer's instructions. As many markers as possible were stained intracellularly to avoid potential issues in detecting key cell surface markers, which could theoretically be masked for detection by the binding of ATGAM to these cell surface markers *in vivo*. Cells were then measured on the Aurora spectral flow cytometer (Cytek Biosciences). For each acquired flow cytometry data file, single, live lymphocytes were gated in OMIQ as shown in **Figure S3**. A median of $0.3 \cdot 10^6$ (range $0.02\text{-}0.5 \cdot 10^6$) single, live lymphocytes were gated for each sample, resulting in a dataset of $9.3 \cdot 10^6$ cells. To compare the cellular composition between samples, $0.1 \cdot 10^6$ cells were selected from each sample by downsampling, and visualized by performing UMAP dimensionality reduction analyses in OMIQ based on 15 neighbors, a minimum distance of 0.3 and 400 epochs. Only for the day 5 sample from patient UPN13 less cells were available ($0.02 \cdot 10^6$ cells), due lymphodepletion caused by ATGAM infusion. CD3, CD19 and anti-horse IgG stainings were not used generate the UMAP due to differences in marker expression intensities between samples. To distinguish all major lymphoid lineages, all single, live lymphocytes were clustered into 150 cell clusters using FlowSOM[7] in OMIQ, which were then merged to 6 clusters based on similarities in marker expression. Major lymphoid lineages were defined as follows: $CD3^+CD4^+$ T-cells, $CD3^+CD8^+$ T-cells, $CD3^+TCR\gamma\delta^+$ T-cells, $FoxP3^+$ regulatory T-cells, $CD3^-CD56^+$ NK-cells and $CD19^+$ B-cells. Analyses at the subpopulation level were performed by manual gating in OMIQ. R version 4.4.1 ran in RStudio version 2023.03 was used for data visualization and analysis.

For detailed characterization of $CD27^+$ B-cells post-ATGAM, cryopreserved PBMCs collected from UPN31 on day 13 after the first ATGAM infusion were stained with a 16-marker spectral flow cytometry antibody panel directed against B-cell surface markers. This panel enabled analysis of B-cell isotype distribution, activation status and expression of complement inhibitors. The panel also incorporated PE- and APC-conjugated tetanus toxoid to allow for

the detection of tetanus-specific B-cells. Cryopreserved PBMC samples from two sex- and age-matched healthy donors (also included in the larger spectral flow cytometry analysis) were included as a reference. Cells were fixed prior to acquisition on the Aurora spectral flow cytometer. Single, live B-cells were gated using the forward and side scatter, and by selecting $CD19^+$ B-cells while excluding all cells positive for the live dead stain. $0.2 \cdot 10^6$ cells single, live B-cells were gated from the day 13 sample from UPN31, while $0.5 \cdot 10^6$ and $1.1 \cdot 10^6$ single, live B-cells were acquired for the controls.

Table S1. Spectral flow cytometry panel for phenotyping of all lymphoid lineages.

Marker	Fluorochrome	Clone	Manufacturer	Dilution	Extracellular / intracellular staining
CD45RA	BUV395	HI100	BD	600	Intracellular
CCR7	BUV563	3D12	BD	100	Extracellular
Tetramers CMV	BUV615	NA	In-house	75	Extracellular
Tetramers EBV	BUV615	NA	In-house	75	Extracellular
CD19	BV421	HIB19	BioLegend	160	Intracellular
CD56	BV510	NCAM16.2	BD	30	Intracellular
CD27	BV570	O323	BioLegend	30	Extracellular
CD38	BV605	HIT2	BD	75	Intracellular
CCR6	BV711	G034E3	BioLegend	40	Extracellular
TCRγδ	BV750	11F2	BD	75	Extracellular
CD24	BV786	ML5	BioLegend	100	Intracellular
Goat anti-horse IgG	AF488	NA	Jackson Immunoresearch	100	Extracellular
CD3	RB545	UCHT1	BD	1000	Intracellular
FoxP3	RB744	259D/C7	BD	75	Intracellular
CD69	RB780	FN50	BD	2000	Intracellular
IgD	PE	IADB6	Beckman Coulter	1000	Extracellular
Tetramers EBV	PE	NA	In-house	100	Extracellular
Granzyme B	PE-CF594	GB11	BD	1500	Intracellular
CD28	PE-Cy5	CD28.2	BD	200	Intracellular
CD8	PE-fire 700	SK1	BioLegend	1000	Intracellular
Ki-67	PE-Cy7	B56	BD	400	Intracellular
CD4	PE-fire 810	SK3	BD	800	Intracellular
IgM	APC	MHM-88	BioLegend	160	Intracellular
Tetramers CMV	APC	NA	In-house	50	Extracellular
KLRG1	Spark NIR 685	SA231A2	BioLegend	50	Intracellular
HLA-DR	AF700	G46-6	BD	75	Intracellular
Live/dead	Zombie-NIR	NA	BioLegend	500	NA
Perforin	APC-fire 750	B-D48	BioLegend	300	Intracellular

Table S2. Model building process for active ATGAM.

Model number	Description	Model	Compared against	OFV	ΔOFV	Comments
1	One-compartment with linear elimination	CL = Θ1 × EXP(IIV) V= Θ2 × EXP(IIV)	-	84.063	-	Additive error fixed to 0.0001 (rounding errors without fixation)
2	One-compartment with parallel linear and non-linear elimination	CL = Θ1 × EXP(IIV) V= Θ2 × EXP(IIV) Vmax= Θ3 × EXP(IIV) Km= Θ4 × EXP(IIV)	1	84.063	0	Additive error fixed to 0.0001
3	Two-compartment with linear elimination	CL = Θ1 × EXP(IIV) Vc = Θ2 × EXP(IIV) Q = Θ3 × EXP(IIV) Vp = Θ4	2	57.611	-26.45	Additive error fixed to 0.0001
4	Two-compartment with linear elimination + IIV V2	CL = Θ1 × EXP(IIV) Vc = Θ2 × EXP(IIV) Q = Θ3 × EXP(IIV) Vp = Θ4 × EXP(IIV)	3	-12.41	-70.02	Additive error fixed to 0.0001 Worse VPC (see **Figure S4**)
4	Two-compartment with linear elimination + OMEGA BLOCK between IIV CL and V1	CL = Θ1 × EXP(IIV) Vc = Θ2 × EXP(IIV) Q = Θ3 × EXP(IIV) Vp = Θ4	3	44.027	-13.58	Additive error fixed to 0.0001
5	Two-compartment with linear elimination + OMEGA BLOCK between IIV CL and V1 + different proportional error ≥60AU/mL and <60AU/mL	CL = Θ1 × EXP(IIV) Vc = Θ2 × EXP(IIV) Q = Θ3 × EXP(IIV) Vp = Θ4	4	34.705	-9.322	**Final model** Additive error fixed to 0.0001 IIV CL: 43.1% IIV Vc: 52% IIV Q: 143.2%
6	Two-compartment with linear elimination + OMEGA BLOCK between IIV CL and V1 + different proportional error ≥60AU/mL and <60AU/mL + bodyweight as covariate	CL = Θ1 × EXP(IIV) × ((WT/MWT)**Θ5) Vc = Θ2 × EXP(IIV) × ((WT/MWT)**Θ6) Q = Θ3 × EXP(IIV) Vp = Θ4	5	35.505	0.8	Additive error fixed to 0.0001 IIV CL: 45.2% IIV Vc: 50.8% IIV Q: 145.9%
7	Two-compartment with linear elimination + OMEGA BLOCK between IIV CL and V1 + different proportional error ≥60AU/mL and <60AU/mL + lymphocyte count pre-ATGAM as covariate	CL = Θ1 × EXP(IIV) × (1+(LYMPH/MLYMPH)*Θ5) Vc = Θ2 × EXP(IIV) Q = Θ3 × EXP(IIV) Vp = Θ4	5	36.813	2.108	Additive error fixed to 0.0001 IIV CL: 42.9% IIV Vc: 50.7% IIV Q: 144.2%
8	Two-compartment with parallel linear and non-linear elimination	CL = Θ1 × EXP(IIV) Vc= Θ2 × EXP(IIV) Vp= Θ3 Vmax= Θ4 × EXP(IIV) Km= Θ5 × EXP(IIV)	-	Model unstable	Model unstable	Additive error fixed to 0.0001

CL indicates clearance; IIV: inter-individual variability; Km: Michaelis-Menten contant; LYMPH: lymphocyte count pre-ATGAM; MLYMPH: median lymphocyte count pre-ATGAM; MWT: median population weight; OFV: objective function value; Q: intercompartmental clearance; V: volume of distribution; Vc: volume of distribution central compartment; Vp: volume of distribution peripheral compartment; Vmax: maximum elimination rate; WT: bodyweight.

Table S3. Model building process for total ATGAM.

Model number	Description	Model	Compared against	OFV	ΔOFV	Comments
1	One-compartment with linear elimination	CL = Θ1 × EXP(IIV) V= Θ2 × EXP(IIV)	-	2026.3	-	Additive error fixed to 0.0001 (rounding errors without fixation)
2	One-compartment with parallel linear and non-linear elimination	CL = Θ1 × EXP(IIV) V= Θ2 × EXP(IIV) Vmax= Θ3 × EXP(IIV) Km= Θ4 × EXP(IIV)	1	2026.4	0.06	Additive error fixed to 0.0001. Model instable.
3	Two-compartment with linear elimination	CL = Θ1 × EXP(IIV) Vc = Θ2 × EXP(IIV) Q = Θ3 × EXP(IIV) Vp = Θ4	1	1937.99	-88.32	Additive error fixed to 0.0001 Model unstable
4	Two-compartment with linear elimination + Vp fixed	CL = Θ1 × EXP(IIV) Vc = Θ2 × EXP(IIV) Vp = Θ4 FIX	3	1940.7	2.72	**Final model** Additive error fixed to 0.0001 IIV CL: 44.0% IIV Vc: 57.2% IIV Q: 290.0%
5	Two-compartment with linear elimination + Vp fixed + OMEGA BLOCK between IIV CL and V1	CL = Θ1 × EXP(IIV) Vc = Θ2 × EXP(IIV) Q = Θ3 × EXP(IIV) Vp = Θ4 FIX	4	1935.9	-4.79	Additive error fixed to 0.0001 IIV CL: 44.2% IIV Vc: 58.1% IIV Q: 303.3%
6	Two-compartment with linear elimination + Vp fixed + bodyweight as covariate	CL = Θ1 × EXP(IIV) × ((WT/MWT)**Θ5) Vc = Θ2 × EXP(IIV) × ((WT/MWT)**Θ6) Q = Θ3 × EXP(IIV) Vp = Θ4	4	1947.2	6.48	Additive error fixed to 0.0001 IIV CL: 50.5% IIV Vc: 59.9% IIV Q: 295.8%
8	Two-compartment with parallel linear and non-linear elimination	CL = Θ1 × EXP(IIV) Vc= Θ2 × EXP(IIV) Vp= Θ3 Vmax= Θ4 × EXP(IIV) Km= Θ5 × EXP(IIV)	-	Model unstable	Model unstable	Additive error fixed to 0.0001

CL indicates clearance; IIV: inter-individual variability; Km: Michaelis-Menten contant; MWT: median population weight; OFV: objective function value; Q: intercompartmental clearance; V: volume of distribution; Vc: volume of distribution central compartment; Vp: volume of distribution peripheral compartment; Vmax: maximum elimination rate; WT: bodyweight.

Table S4. Model estimates for active ATGAM pharmacokinetic parameters.

Parameter	Median (range)	Mean	RSE (%)	Shrinkage	1000 bootstrap run results	
					Median	95% CI
Clearance (CL in L/day)	6.5 (3.4-24.0)	6.97	11%		7.02	5.07 - 9.80
Volume of distribution of central compartment (V_c in L)	1.5 (0.6-4.2)	1.51	17%		1.51	0.88 - 2.86
Intercompartmental clearance (Q in L/day)	2.3 (0.5-65.2)	3.2	38%		3.32	1.32 - 9.18
Volume of distribution of peripheral compartment (V_p in L)	11.3	11.2	12%		11.56	6.51 - 22.94
Inter-individual variability (IIV)						
Clearance (IIV CL, %)		43.1	13%	9%	41.98	31.01 - 53.62
CL ~ V_c (%)		-	-	-	39.26	15.72 - 56.14
Volume of distribution of central compartment (IIV Vc, %)		52	16%	22%	49.48	28.36 - 68.12
Intercompartmental clearance (IIV Q, %)		143.2	17%	8%	141.75	102.51 - 194.50
Random residual variability						
Proportional error (CV%)		0.3	12%		0.30	0.23 - 0.57
Additional error (AU/mL)		0.0001	fixed		0.0001	0.0001 - 0.0001
Half-life distribution phase (days)	0.09 (0.02-0.25)					
Half-life elimination phase (days)	4.5 (0.5-16.1)					
Peak concentration (C_{max} in AU/mL)	668.1 (208.6-1595.9)					
Total exposure (AUC_{0-inf})	1801.2 (583.9-4218.7)					

Table S5. Model estimates for total ATGAM pharmacokinetic parameters.

Parameter	Median (range)	Mean	RSE (%)	Shrinkage	1000 bootstrap run results	
					Median	95% CI
Clearance (CL in L/day)	0.4 (0.2-1.4)	0.426	8%		0.42	0.36 - 0.50
Volume of distribution of central compartment (V_c in L)	3.3 (0.9-8.7)	3.22	8%		3.17	2.65 - 3.67
Intercompartmental clearance (Q in L/day)	0.1 (0.0006-2.7)	0.032	12%		0.03	0.01 - 0.15
Volume of distribution of peripheral compartment (V_p in L)	0.9	0.949	fixed		0.95	0.95 - 0.95
Inter-individual variability (IIV)						
Clearance (IIV CL, %)		44	14%	10%	43.10	28.65 - 55.37
Volume of distribution of central compartment (IIV Vc, %)		57.2	10%	4%	57.10	46.13 - 69.76
Intercompartmental clearance (IIV Q, %)		290	17%	41%	276.86	137.16 - 402.10
Random residual variability						
Proportional error (CV%)		0.355	10%		0.35	0.28 - 0.42
Additional error (ug/mL)		0.0001	fixed		0.0001	0.0001 - 0.0001
Half-life distribution phase (days)	4.3 (0.2-8.9)					
Half-life elimination phase (days)	16.8 (1.8-1015.9)					
Peak concentration (C_{max} in µg/mL)	2500.7 (1175.4-7649.0)					
Total exposure ($AUC_{0\text{-}inf}$)	28160.5 (9761.4-90999.0)					

Table S6. Patient characteristics by active ATGAM exposure groups.

Characteristic	Low active ATGAM exposure (n=15)	Medium active ATGAM exposure (n=14)	High active ATGAM exposure (n=15)	P-value
Age at diagnosis (median in years)	40	60	57	0.21
Sex (n)				0.32
Male	7	8	11	
Female	8	6	4	
Disease severity at diagnosis (n)				0.91
Non-severe AA	2	3	2	
Severe AA	7	7	9	
Very severe AA	6	4	4	
Weight at diagnosis (median in kg)	71	75	88	0.003
Height (median in cm)	170	173	180	0.003
Body mass index at diagnosis (median)	22.4	24.5	26.0	0.33
Neutrophils pre-ATGAM (median in 10^9/L)	0.33	0.24	0.31	>0.9
Reticulocytes pre-ATGAM (median in 10^9/L)	17.5	8.4	10	0.6
Lymphocytes pre-ATGAM (median in 10^6/L)[a]	1625	1485	1315	0.75
Eltrombopag added to IST (n)	5	3	8	0.11
Eltrombopag added with start ATGAM	3	2	2	
Eltrombopag added 20-180 days post-ATGAM	2: Day 96 Day 100	1: Day 92	7: Day 69 Day 86 Day 138 Day 160 Day 163 Day 165	
Other second-line treatment ≤180 days post-ATGAM	0	0	0	1.0
Ciclosporin discontinued ≤180 days post-ATGAM	0	0	1	0.40
Deaths ≤180 days post-ATGAM	2	1	1	0.78

[a]Data missing for 2 AA patients (1 in low and 1 in high exposure groups). Statistical differences between continuous variables calculated by Kruskal Wallis test. Statistical differences between categorical variables calculated by Fisher's Exact test. Statistical differences in addition of eltrombopag to IST, ciclosporin discontinuation and death calculated by log-rank (survival) test.

Final active ATGAM pharmacokinetic model code

```
$PROBLEM PK

$INPUT ID TIME DV TAD ATGNR C AMT RATE MDV EVID WEIGHT HEIGHT LYMPHO
CD4 CD8 NK B MONO dose_code ATGMgKg DaysATG ATGMgKgDay DayATGStart AGE
GENDER RESPONSE_3M RESPONSE_6M BMI

$DATA PK_ATGAM_data_ACTIVE.csv  IGNORE=@

$SUBROUTINES ADVAN6 TOL=3

$MODEL
COMP=(CENTRAL DEFOBS DEFDOSE)
COMP=(PERIPH)
COMP= AUC

$PK
CL = THETA(1) * EXP(ETA(1))
V1 = THETA(2) * EXP(ETA(2))
Q  = THETA(3) * EXP(ETA(3))
V2 = THETA(4)
S1 = V1
K10=CL/V1
K12=Q/V1
K21=Q/V2

$DES
C1=A(1)/V1
DADT(1)=-K10*A(1)-K12*A(1)+K21*A(2)
DADT(2)=-K21*A(2)+K12*A(1)
DADT(3)= C1

$ERROR
IPRED = F
IF(DV.GE.60) W = SQRT(THETA(5)**2*IPRED**2 + THETA(6)**2)
IF(DV.LT.60) W = SQRT(THETA(7)**2*IPRED**2 + THETA(6)**2)
   Y = IPRED + W*EPS(1)
 IRES = DV-IPRED
IWRES = IRES/W
AUC = A(3)
AUCCL = AMT/CL

$THETA
(0, 6.97) ; CL
(0, 1.51) ; V1
(0, 3.2) ; Q
(0, 11.2) ; V2
(0, 0.3) ; Prop.RE (sd)
(0.0001) FIX ; Add.RE (sd)
(0, 0.579) ; Prop.RE (sd)
```

```
$OMEGA BLOCK(2)
 0.186  ; IIV CL
 0.18 0.27  ; IIV V1
$OMEGA
 2.05 ; IIV Q

$SIGMA
 1 FIX  ; Proportional error PK

$EST METHOD=1 INTER MAXEVAL=2000 NOABORT SIG=2 PRINT=1 POSTHOC
$COV

; Xpose
$TABLE CL V1 V2 Q ID TIME DV MDV EVID PRED IPRED IWRES CWRES ETA1 ETA2
ETA3 LYMPHO CD4 CD8 B NK MONO AGE GENDER WEIGHT HEIGHT BMI AUCCL AUC
Response_3M Response_6M ONEHEADER NOPRINT FILE=sdtab002.3aa
$TABLE CL V1 ID TIME DV MDV EVID PRED IPRED IWRES CWRES ETA1 ETA2 ETA3
LYMPHO CD4 CD8 B NK MONO AGE GENDER WEIGHT HEIGHT AUCCL AUC
Response_3M Response_6M ONEHEADER NOPRINT FIRSTONLY FILE=patab002.3aa
```

Final total ATGAM pharmacokinetic model code

```
$PROBLEM PK

$INPUT ID TIME DV TAD ATGNR C AMT RATE MDV EVID WEIGHT HEIGHT LYMPH CD4
CD8 NK B MONO dose_code ATGMgKg DaysATG ATGMgKgDay DayATGStart AGE
GENDER RESPONSE_3M RESPONSE_6M

$DATA PK_ATGAM_data_TOTAL.csv  IGNORE=@

$SUBROUTINES ADVAN6 TOL=3

$MODEL
COMP=(CENTRAL DEFOBS DEFDOSE)
COMP=(PERIPH)
COMP= AUC

$PK
TVCL = THETA(1)
CL = TVCL * EXP(ETA(1))

TVV1 = THETA(2)
V1 = TVV1 * EXP(ETA(2))

TVQ = THETA(3)
Q  = TVQ * EXP(ETA(3))

TVV2 = THETA(4)
V2 = TVV2

S1 = V1

K10=CL/V1
K12=Q/V1
K21=Q/V2

$DES
C1=A(1)/V1
DADT(1)=-K10*A(1)-K12*A(1)+K21*A(2)
DADT(2)=-K21*A(2)+K12*A(1)
DADT(3)= C1

$ERROR
IPRED = F
   W = SQRT(THETA(5)**2*IPRED**2 + THETA(6)**2)
   Y = IPRED + W*EPS(1)
 IRES = DV-IPRED
IWRES = IRES/W
AUC = A(3)
AUCCL = AMT/CL
```

```
$THETA
(0, 0.424) ; CL
(0, 3.23) ; V1
(0, 0.0299) ; Q
(0.949) FIX ; V2
(0, 0.353) ; Prop.RE (sd)
(0.00001) FIX ; Add.RE (sd)

$OMEGA
 0.194 ; IIV CL
 0.318 ; IIV V1
 8.74 ; IIV Q

$SIGMA
 1 FIX  ; Proportional error PK

$EST METHOD=1 INTER MAXEVAL=2000 NOABORT SIG=2 PRINT=1 POSTHOC
$COV

; Xpose
$TABLE CL V1 V2 Q ID TIME DV MDV EVID PRED IPRED IWRES CWRES ETA1 ETA2
ETA3 LYMPH CD4 CD8 B NK MONO AGE GENDER WEIGHT HEIGHT AUCCL AUC
Response_3M Response_6M ONEHEADER NOPRINT FILE=sdtab005.3.2b3
$TABLE CL V1 V2 Q ETA1 ETA2 ETA3 LYMPH CD4 CD8 B NK MONO AGE GENDER
WEIGHT HEIGHT ONEHEADER NOPRINT FIRSTONLY FILE=patab005.3.2b3
```

References

1. Regan JF, Lyonnais C, Campbell K, Smith LV, Buelow R, Group USTM-CS. Total and active thymoglobulin levels: effects of dose and sensitization on serum concentrations. Transpl Immunol. 2001;9(1):29-36.
2. Rebello P, Hale G. Pharmacokinetics of CAMPATH-1H: assay development and validation. J Immunol Methods. 2002;260(1-2):285-302.
3. Jol-van der Zijde CM, Bredius RG, Jansen-Hoogendijk AM, et al. IgG antibodies to ATG early after pediatric hematopoietic SCT increase the risk of acute GVHD. Bone Marrow Transplant. 2012;47(3):360-368.
4. Oostenbrink LVE, Von Asmuth EGJ, Jol-van der Zijde CM, et al. Anti-T-lymphocyte globulin exposure is associated with acute graft-versus-host disease and relapse in pediatric acute lymphoblastic leukemia patients undergoing hematopoietic stem cell transplantation: a multinational prospective study. Haematologica. 2024;109(9):2854-2863.
5. Bergstrand M, Hooker AC, Wallin JE, Karlsson MO. Prediction-corrected visual predictive checks for diagnosing nonlinear mixed-effects models. AAPS J. 2011;13(2):143-151.
6. Comets E, Lavenu A, Lavielle M. Parameter Estimation in Nonlinear Mixed Effect Models Using saemix, an R Implementation of the SAEM Algorithm. J Stat Softw. 2017;80(3):1-41.
7. Van Gassen S, Callebaut B, Van Helden MJ, et al. FlowSOM: Using self-organizing maps for visualization and interpretation of cytometry data. Cytometry A. 2015;87(7):636-645.

Figure S1

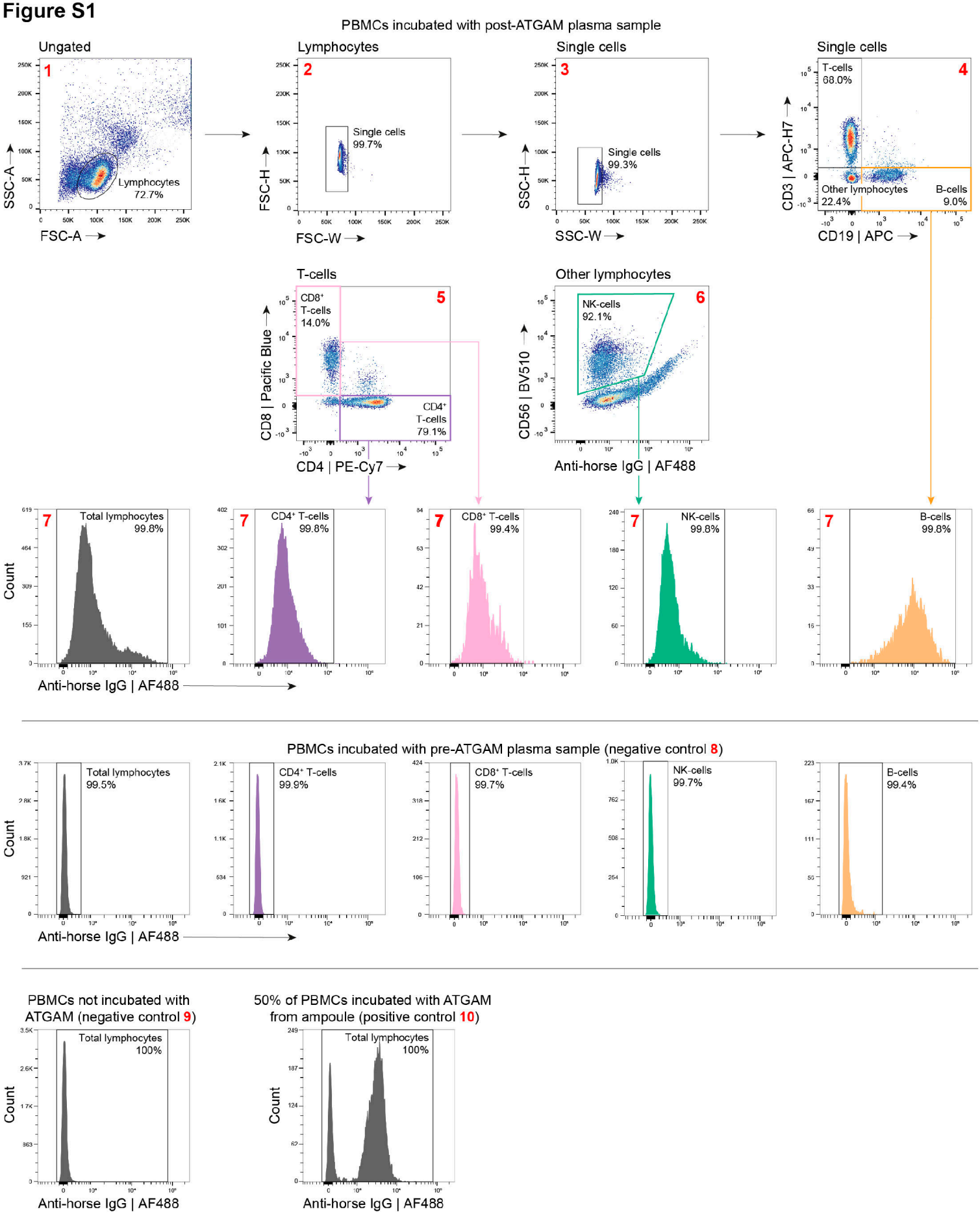
PBMCs incubated with post-ATGAM plasma sample
Ungated
1
Lymphocytes 72.7%
SSC-A
FSC-A
Lymphocytes
2
Single cells 99.7%
FSC-H
FSC-W
Single cells
3
Single cells 99.3%
SSC-H
SSC-W
Single cells
4
T-cells 68.0%
Other lymphocytes 22.4%
B-cells 9.0%
CD3 | APC-H7
CD19 | APC
T-cells
5
CD8+ T-cells 14.0%
CD4+ T-cells 79.1%
CD8 | Pacific Blue
CD4 | PE-Cy7
Other lymphocytes
6
NK-cells 92.1%
CD56 | BV510
Anti-horse IgG | AF488
7
Total lymphocytes 99.8%
CD4+ T-cells 99.8%
CD8+ T-cells 99.4%
NK-cells 99.8%
B-cells 99.8%
Count
Anti-horse IgG | AF488
PBMCs incubated with pre-ATGAM plasma sample (negative control 8)
Total lymphocytes 99.5%
CD4+ T-cells 99.9%
CD8+ T-cells 99.7%
NK-cells 99.7%
B-cells 99.4%
PBMCs not incubated with ATGAM (negative control 9)
Total lymphocytes 100%
50% of PBMCs incubated with ATGAM from ampoule (positive control 10)
Total lymphocytes 100%

Figure S1. Gating strategy for quantification of active ATGAM plasma concentrations. Lymphocytes were gated using the forward and side scatter (panel 1). Doublets were excluded, and single lymphocytes were selected for further analysis (panels 2-3). Within the single lymphocytes, $CD3^+$ T-cells, $CD19^+$ B-cells or $CD3^-CD19^-$ other lymphocytes were identified (panel 4). $CD4^+$ T-cells and $CD8^+$ T-cells were identified within the T-cell gate (panel 5). $CD56^+$ NK-cells were identified within the 'other lymphocyte' gate (panel 6). The geometric mean fluorescence intensity for the Alexa Fluor 488 anti-horse IgG antibody was determined for each gated population (panels 7). This was used to calculate the active ATGAM concentrations in the patient plasma sample using a reference curve obtained by exposing PBMCs to known concentrations of ATGAM. The gating strategy is shown for PBMCs incubated with a representative post-ATGAM patient plasma sample. Negative controls were included in each experiment and included PBMCs incubated with pre-ATGAM patient plasma samples (panels 8) and PBMCs not exposed to ATGAM (panel 9). Positive controls were PBMCs exposed to known concentrations of ATGAM (panel 10).

Figure S2

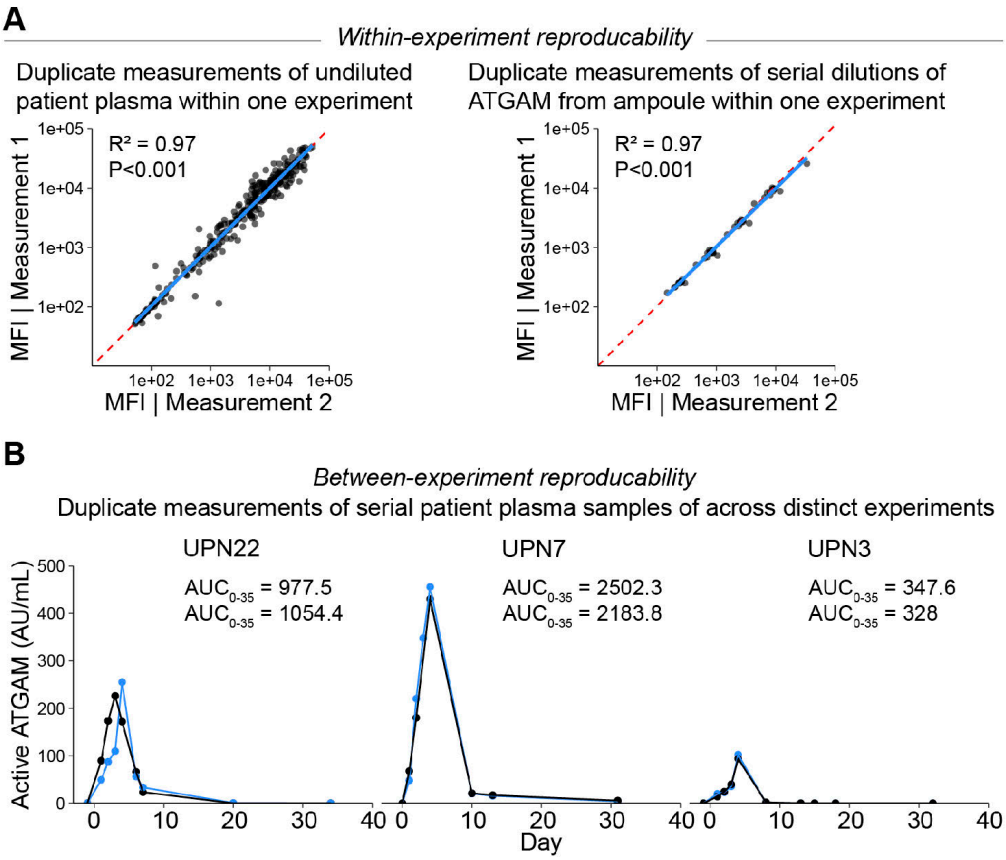

Figure S2. Reproducability and robustness of the active ATGAM assay. [A] Within-experiment reproducability, shown by correlation plot of duplicate measurements of undiluted patient plasma within a single experiment (left), or duplicate measurements of serial dilutions of ATGAM (right). **[B]** Between-experiment reproducability, shown by duplicate measurements of active ATGAM concentrations in patient plasma in independent experiments.

Figure S3

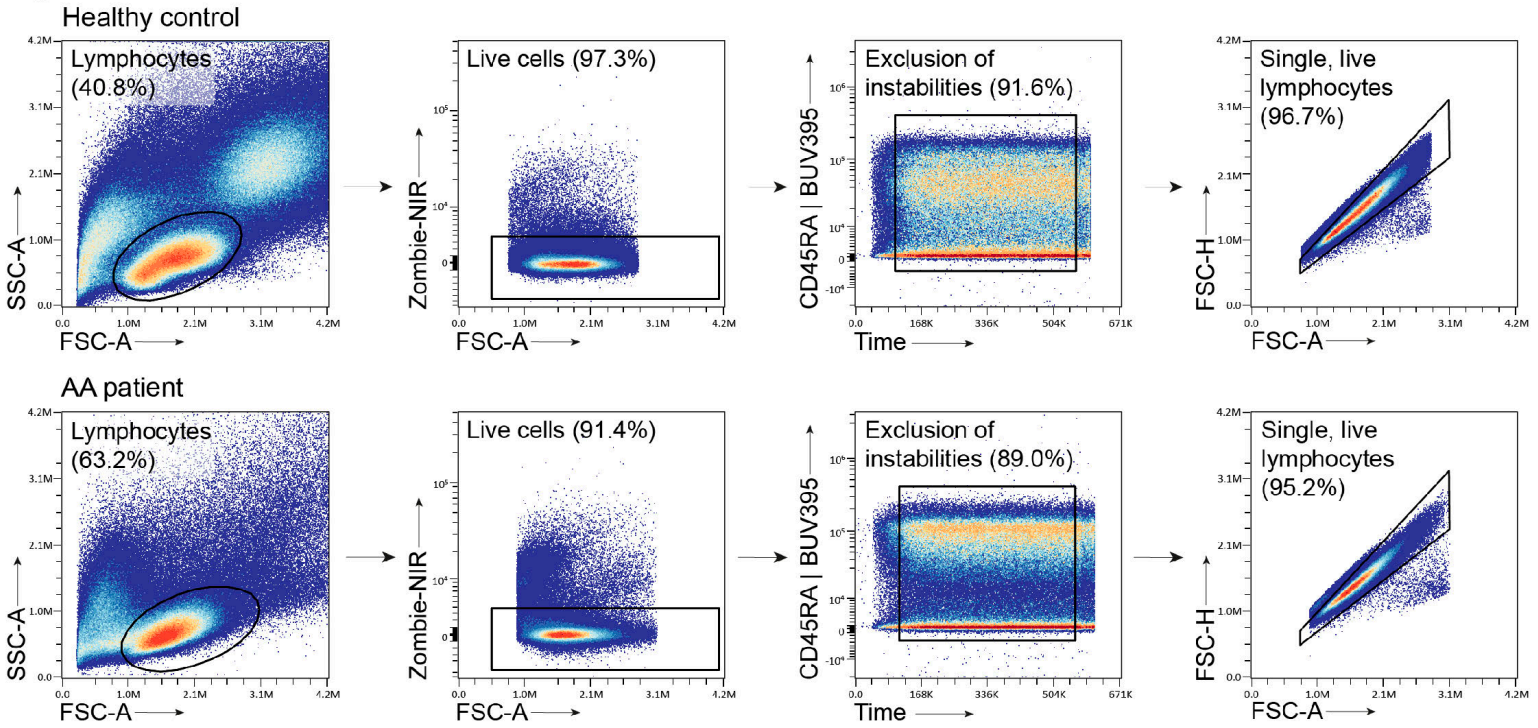

Figure S3. Gating strategy for selection of single, live lymphocytes from spectral flow cytometry data. Lymphocytes were gated in OMIQ based on the forward and side scatter (panel 1). Next, live cells were identified by selecting cells negative for Zombie-NIR (panel 2), and acquisition instabilities were removed by excluding events recorded at the beginning or end of each measurement (panel 3). Finally, doublets were excluded using the forward scatter height (FSC-H) and forward scatter area (FSC-A) parameters (panel 4). Data for a representative healthy control and aplastic anemia patient are shown. Single, live lymphocytes gated in panel 4 were selected for downstream analyses.

Figure S4

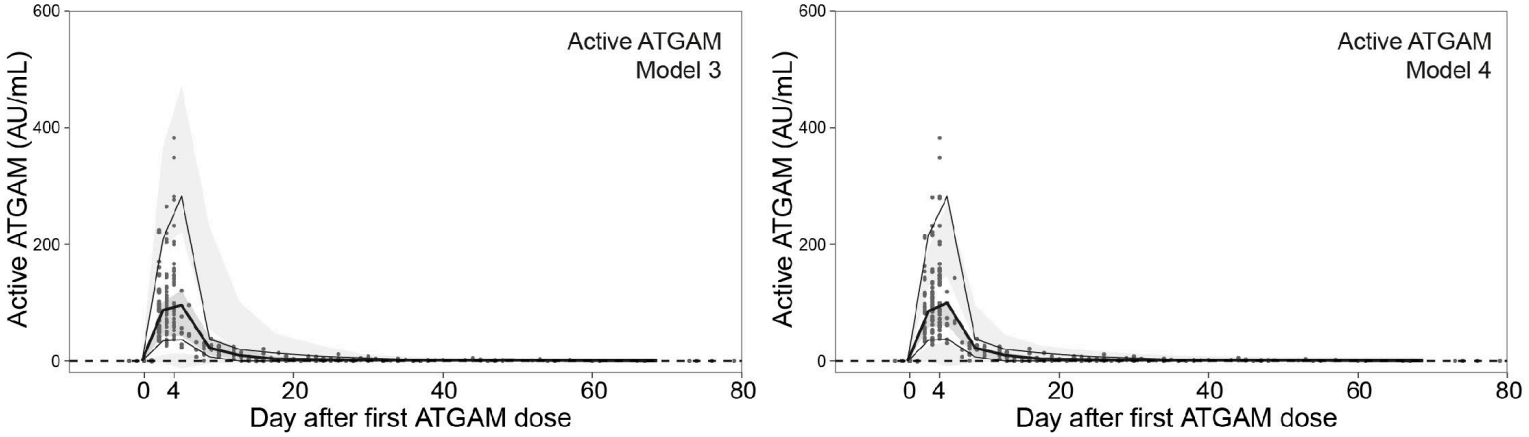

Figure S4. Visual predictive checks for population pharmacokinetic model 3 and model 4 for active ATGAM. Prediction-corrected visual predictive check (VPC) for the final model for active ATGAM. Black lines represent the predicted active ATGAM concentrations at the 95th, 50th, and 5th percentiles. Shaded light gray areas indicate the 95% confidence intervals for the predicted 5th and 95th percentiles, while the dark gray shaded area represents the 95% confidence interval for the predicted 50th percentile. Observed active ATGAM concentrations in all 44 AA patients are shown by black dots.

Figure S5

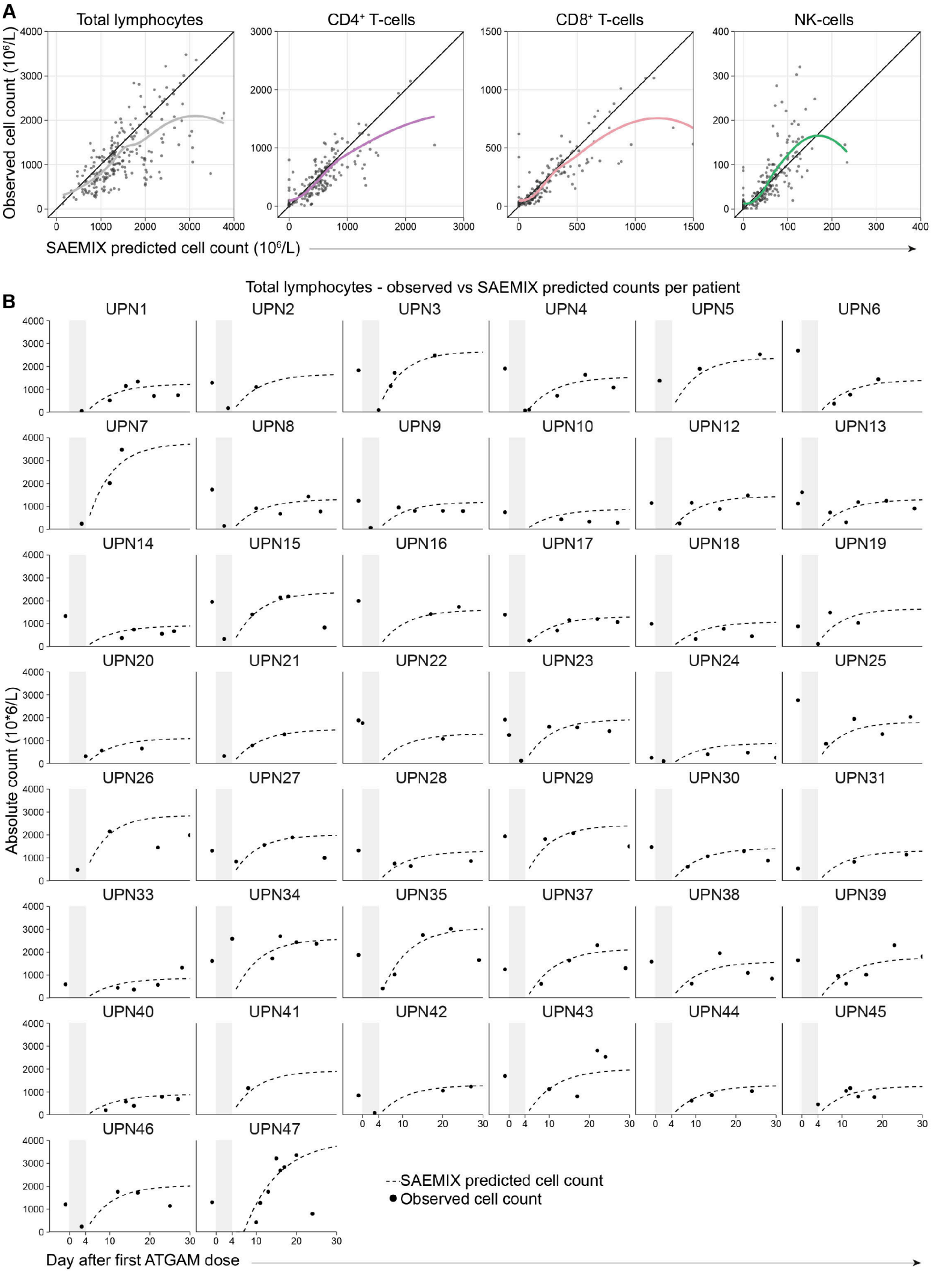
A
Total lymphocytes
CD4⁺ T-cells
CD8⁺ T-cells
NK-cells
Observed cell count (10⁶/L)
SAEMIX predicted cell count (10⁶/L)
B
Total lymphocytes - observed vs SAEMIX predicted counts per patient
UPN1
UPN2
UPN3
UPN4
UPN5
UPN6
UPN7
UPN8
UPN9
UPN10
UPN12
UPN13
UPN14
UPN15
UPN16
UPN17
UPN18
UPN19
UPN20
UPN21
UPN22
UPN23
UPN24
UPN25
UPN26
UPN27
UPN28
UPN29
UPN30
UPN31
UPN33
UPN34
UPN35
UPN37
UPN38
UPN39
UPN40
UPN41
UPN42
UPN43
UPN44
UPN45
UPN46
UPN47
Absolute count (10*6/L)
SAEMIX predicted cell count
Observed cell count
Day after first ATGAM dose

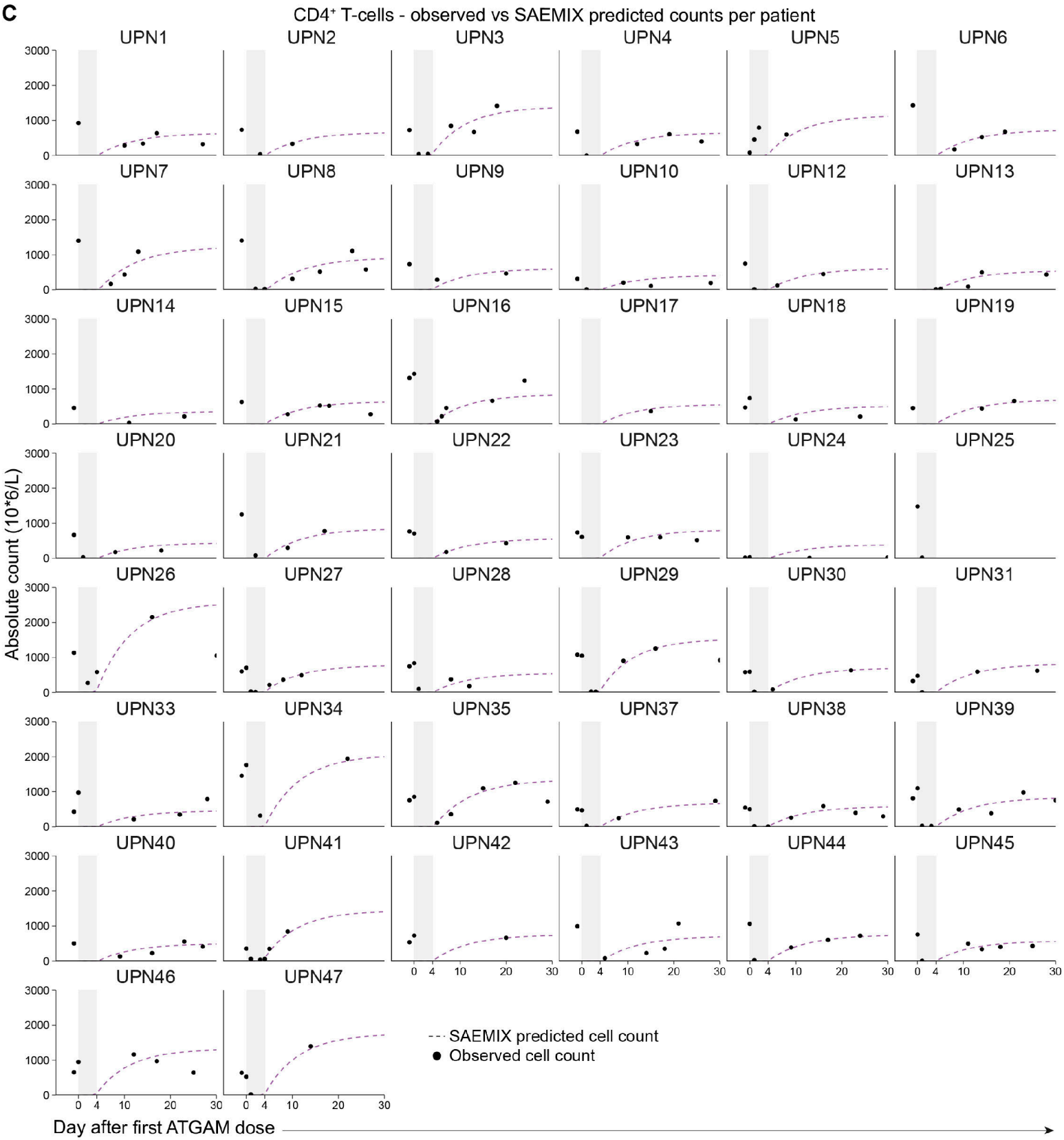
C
CD4⁺ T-cells - observed vs SAEMIX predicted counts per patient
UPN1
UPN2
UPN3
UPN4
UPN5
UPN6
UPN7
UPN8
UPN9
UPN10
UPN12
UPN13
UPN14
UPN15
UPN16
UPN17
UPN18
UPN19
UPN20
UPN21
UPN22
UPN23
UPN24
UPN25
UPN26
UPN27
UPN28
UPN29
UPN30
UPN31
UPN33
UPN34
UPN35
UPN37
UPN38
UPN39
UPN40
UPN41
UPN42
UPN43
UPN44
UPN45
UPN46
UPN47
Absolute count (10*6/L)
0
1000
2000
3000
0
4
10
20
30
SAEMIX predicted cell count
Observed cell count
Day after first ATGAM dose

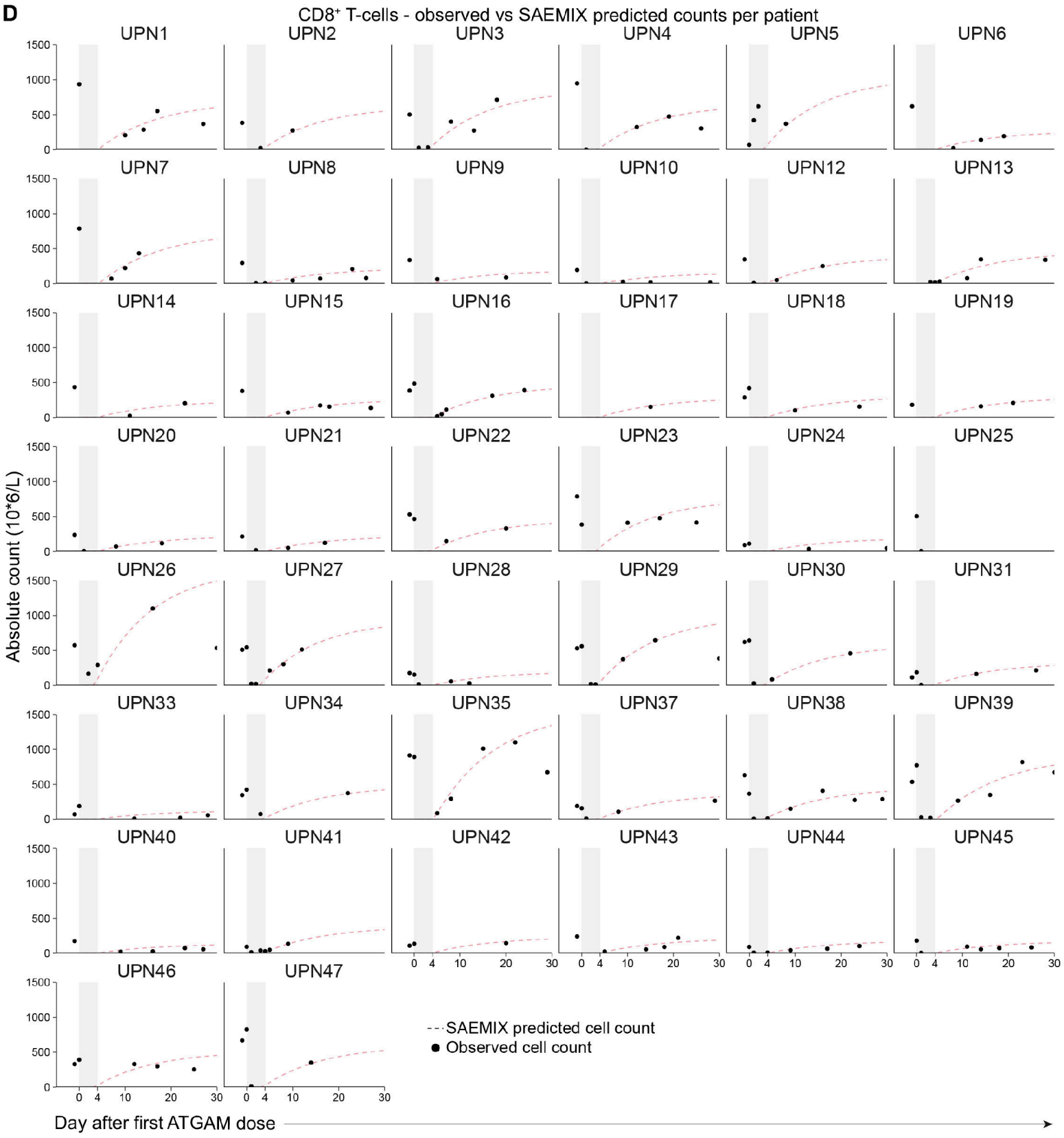
D
CD8⁺ T-cells - observed vs SAEMIX predicted counts per patient
UPN1
UPN2
UPN3
UPN4
UPN5
UPN6
UPN7
UPN8
UPN9
UPN10
UPN12
UPN13
UPN14
UPN15
UPN16
UPN17
UPN18
UPN19
UPN20
UPN21
UPN22
UPN23
UPN24
UPN25
UPN26
UPN27
UPN28
UPN29
UPN30
UPN31
UPN33
UPN34
UPN35
UPN37
UPN38
UPN39
UPN40
UPN41
UPN42
UPN43
UPN44
UPN45
UPN46
UPN47
Absolute count (10*6/L)
0
500
1000
1500
0 4 10 20 30
SAEMIX predicted cell count
Observed cell count
Day after first ATGAM dose

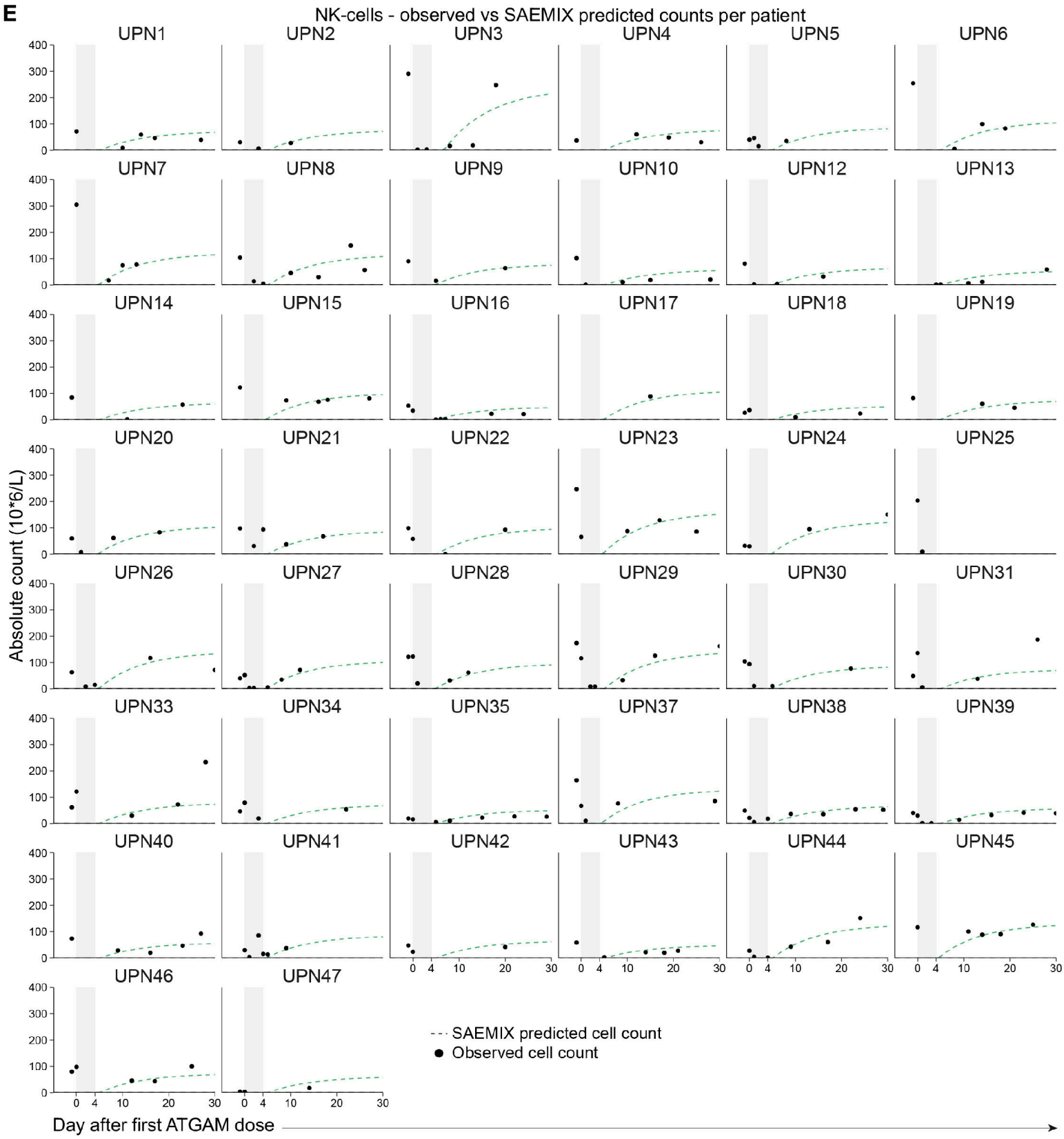

Figure S5. Observed versus predicted immune reconstitution data. [A] Observed versus SAEMIX-predicted total lymphocyte, $CD4^{+}$ T-cell, $CD8^{+}$ T-cell and NK-cell counts shown for all patients. The trend between observed and predicted counts are shown using loess regression. **[B-D]** Observed versus SAEMIX-predicted total lymphocyte **[B]**, $CD4^{+}$ T-cell **[C]**, $CD8^{+}$ T-cell **[D]** and NK-cell **[E]** counts per patient. Dots in present observed lymphocyte counts; dotted lines present predictions.

Figure S6

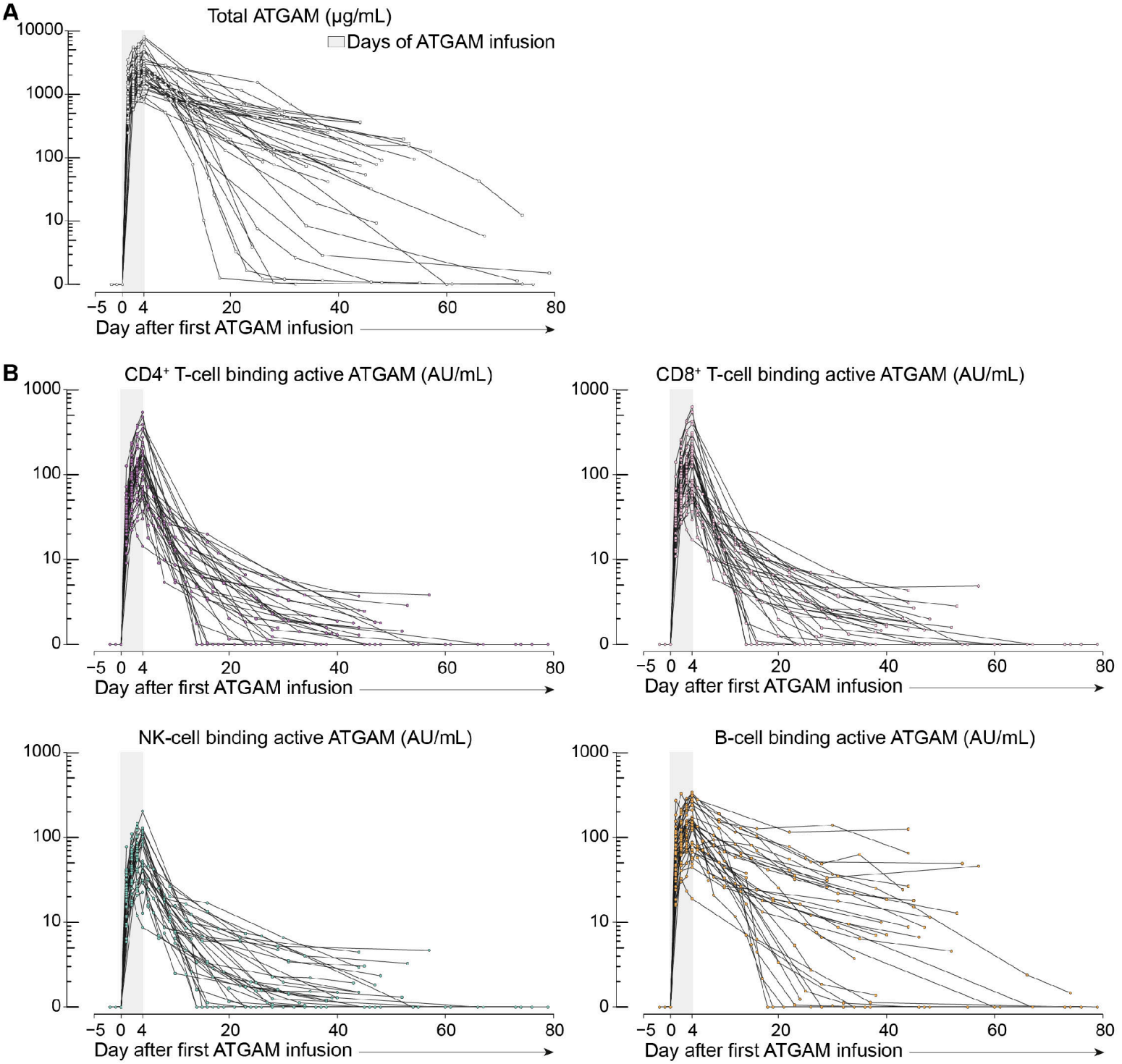

Figure S6. Concentration-time profile of total ATGAM and lineage-binding active ATGAM in patient plasma. [A] Measured total ATGAM, or **[B]** measured CD4⁺ T-cell-binding active ATGAM, CD8⁺ T-cell-binding active ATGAM, CD19⁺ B-cell-binding active ATGAM, and NK-cell binding active ATGAM concentrations in patient plasma (in µg/mL or arbitrary units/mL; n=44 patients) over time before, during and after ATGAM infusion on days 0-4, shown on a logarithmic scale.

Figure S7

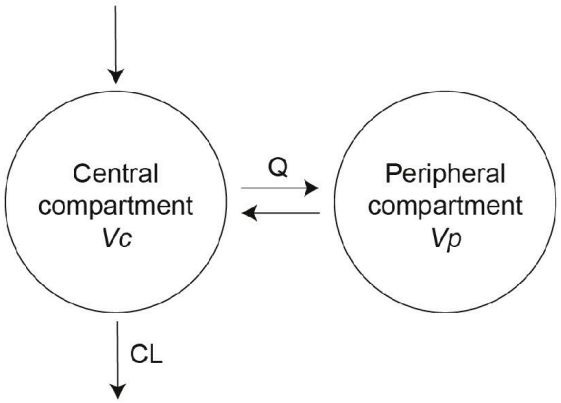

Figure S7. Population pharmacokinetic model overview. A two-compartment population pharmacokinetic model best described the total and active ATGAM concentration-time data. CL: linear clearance, Q: intercompartmental clearance between central compartment with volume Vc, and peripheral compartment with volume Vp.

Figure S8

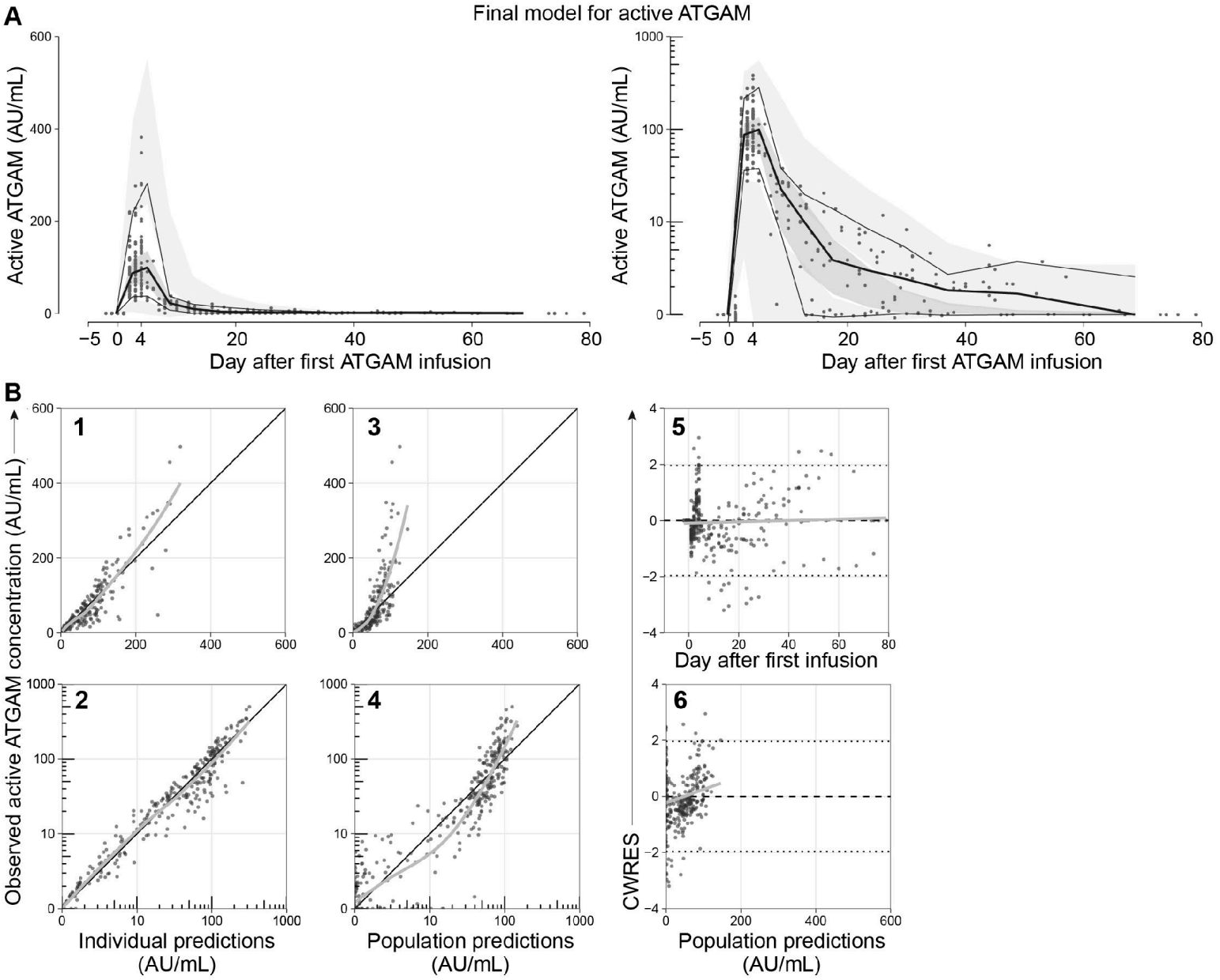

Figure S8. Prediction-corrected visual predictive check and goodness of fit plots for the final pharmacokinetic model for active ATGAM. [A] Prediction-corrected visual predictive check (VPC) for the final model for active ATGAM. Black lines represent the predicted active ATGAM concentrations at the 95th, 50th, and 5th percentiles. Shaded light gray areas indicate the 95% confidence intervals for the predicted 5th and 95th percentiles, while the dark gray shaded area represents the 95% confidence interval for the predicted 50th percentile. Observed active ATGAM concentrations in all 44 AA patients are shown by black dots. VPC is shown on a linear (left) or a logarithmic (right) scale. **[B]** Goodness of fit plots for the final model for active ATGAM. Observed versus individual predicted (IPRED) active ATGAM concentrations on a linear (1) and logarithmic (2) scale; observed versus population predicted (PRED) active ATGAM concentrations on a linear (3) and logarithmic (4) scale; conditional weighted residuals (CWRES) versus time after ATGAM infusion on days 0-4 (5); conditional weighted residuals (CWRES) versus population predicted active ATGAM concentrations (6). Dotted lines in (5) and (6) present the +/- 1.96 ranges of CWRES (95% confidence interval), which should include 95% of the CWRES values.

Figure S9

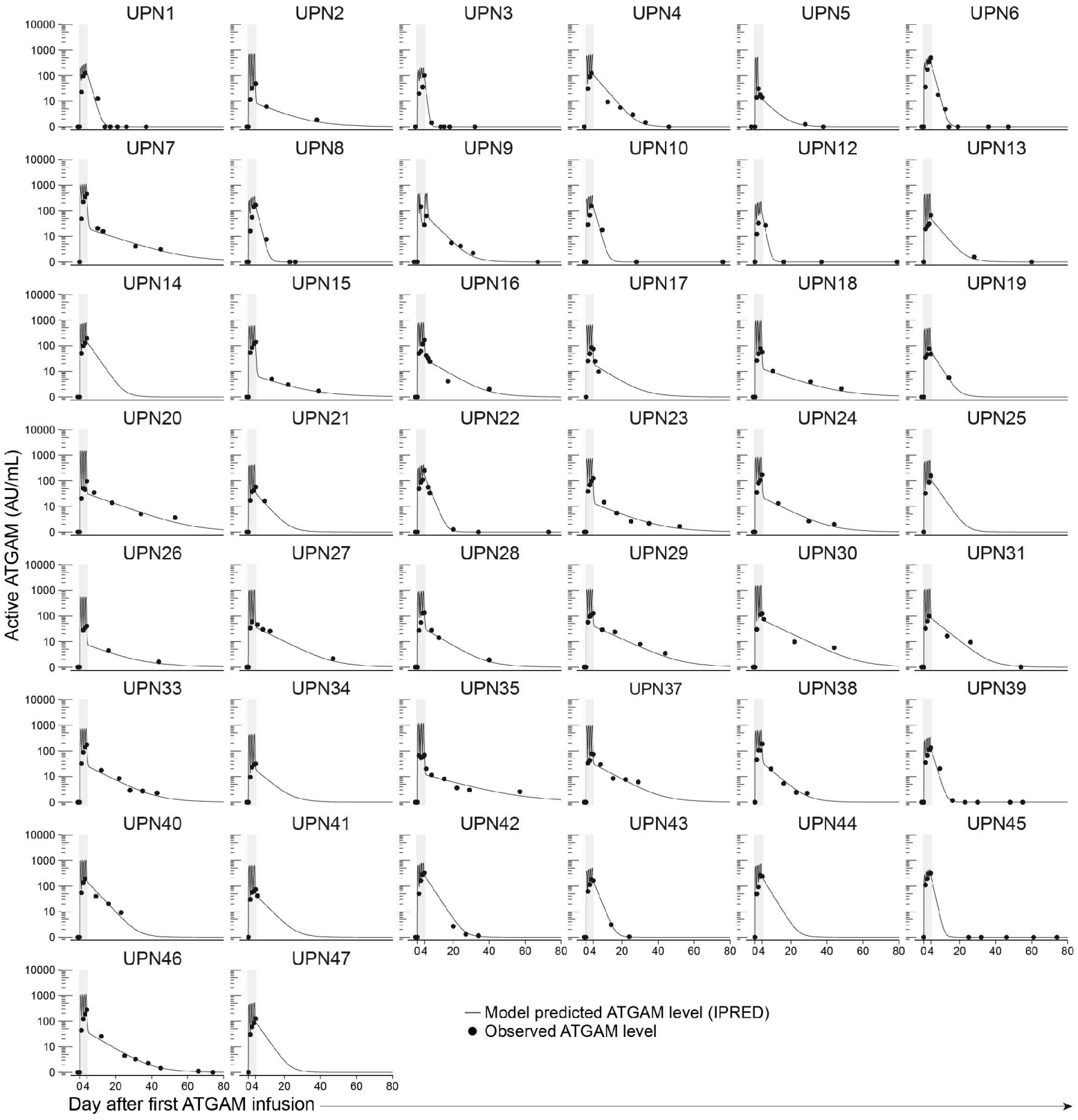

Figure S9. Observed versus model-predicted active ATGAM concentrations per patient. Observed active ATGAM concentrations are shown by black dots, while modelled active ATGAM concentrations in time are shown using black lines. Data are presented on a logarithmic axis.

Figure S10

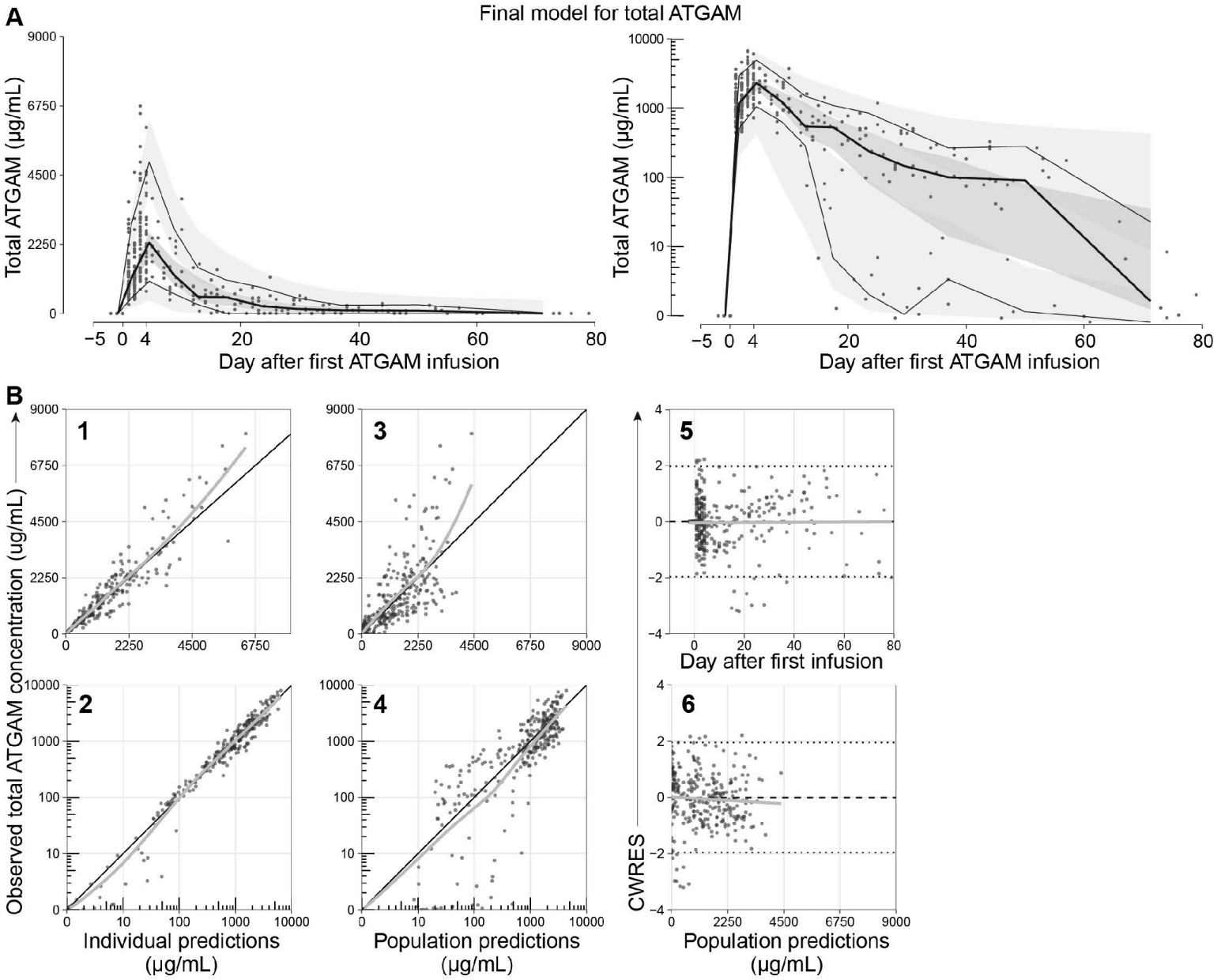

Figure S10. Prediction-corrected visual predictive check and goodness of fit plots for the final pharmacokinetic model for total ATGAM. [A] Prediction-corrected visual predictive check (VPC) for the final model for total ATGAM. Black lines represent the predicted total ATGAM concentrations at the 95th, 50th, and 5th percentiles. Shaded light gray areas indicate the 95% confidence intervals for the predicted 5th and 95th percentiles, while the dark gray shaded area represents the 95% confidence interval for the predicted 50th percentile. Observed total ATGAM concentrations in all 44 AA patients are shown by black dots. VPC is shown on a linear (left) or a logarithmic (right) scale. **[B]** Goodness of fit plots for the final model for total ATGAM. Observed versus individual predicted (IPRED) total ATGAM concentrations on a linear (1) and logarithmic (2) scale; observed versus population predicted (PRED) total ATGAM concentrations on a linear (3) and logarithmic (4) scale; conditional weighted residuals (CWRES) versus time after ATGAM infusion on days 0-4 (5); conditional weighted residuals (CWRES) versus population predicted total ATGAM concentrations (6). Dotted lines in (5) and (6) present the +/- 1.96 ranges of CWRES (95% confidence interval), which should include 95% of the CWRES values.

Figure S11

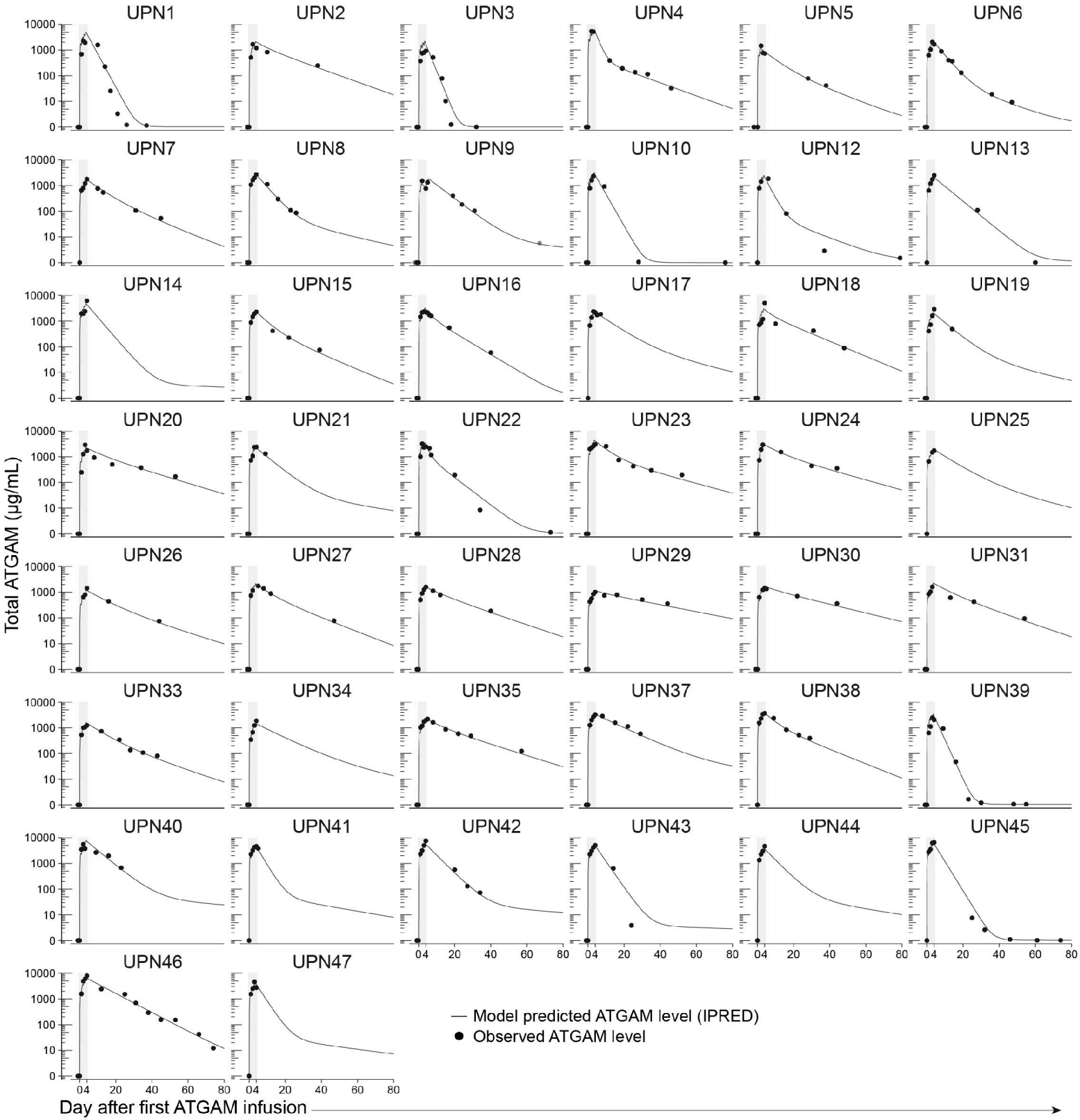

Figure S11. Observed versus model-predicted total ATGAM concentrations per patient. Observed total ATGAM concentrations are shown by black dots, while modelled total ATGAM concentrations in time are shown using black lines. Concentrations are presented on a logarithmic axis.

Figure S12

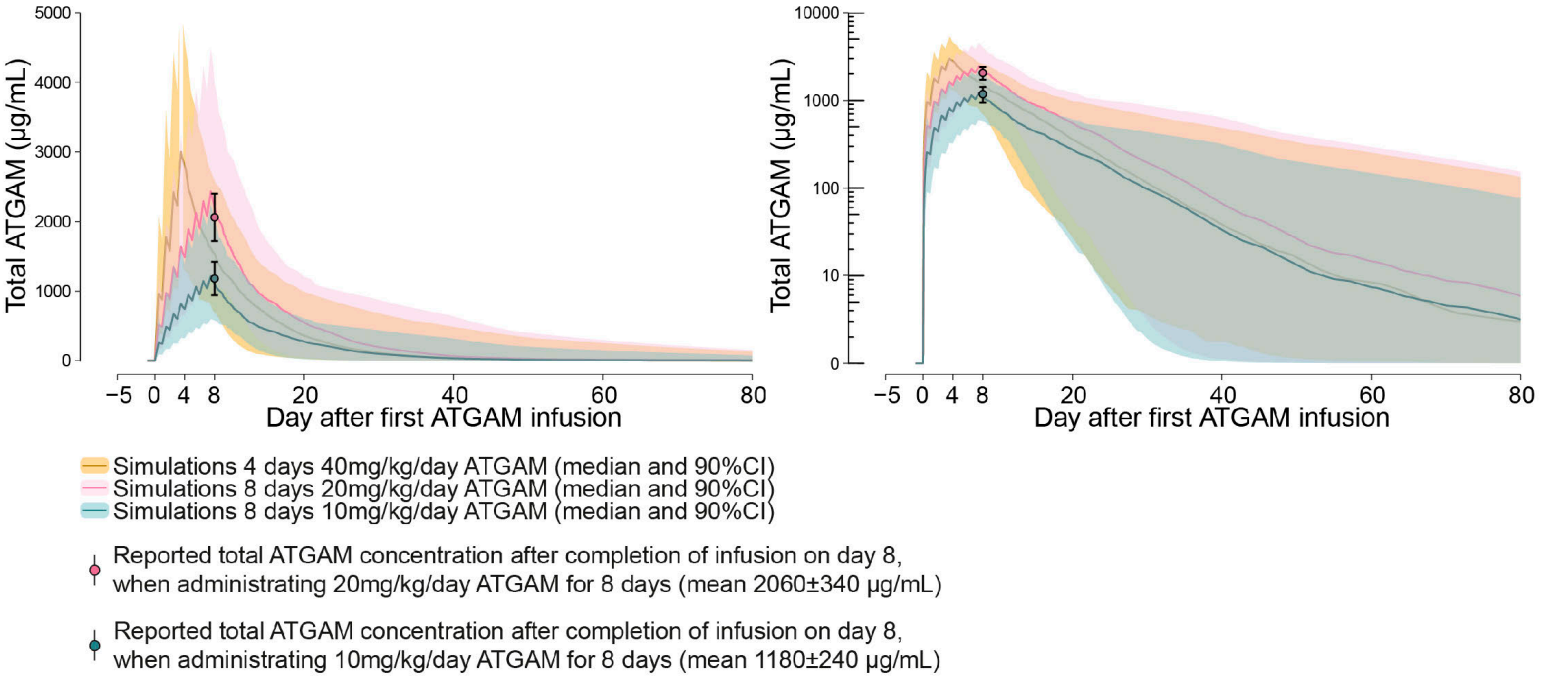

Figure S12. Model simulations for alternative ATGAM dosing schemes. The final pharmacokinetic model for total ATGAM was used to simulate the concentration-time profile of total ATGAM in time after the administration of 8 consecutive days 10mg/kg/day ATGAM, 8 consecutive days 20mg/kg/day ATGAM or 4 consecutive days 40mg/kg/day ATGAM. Lines and shaded areas represent the median and 90% confidence interval obtained from 100 simulations. Dots and error bars represent the mean and range of reported ATGAM peak concentrations following the completion of infusion on day 8 when ATGAM was administered at 10mg/kg/day ATGAM or 20mg/kg/day ATGAM for 8 consecutive days (reported concentrations are described in the manufacturer's brochure by Pfizer).

Figure S13

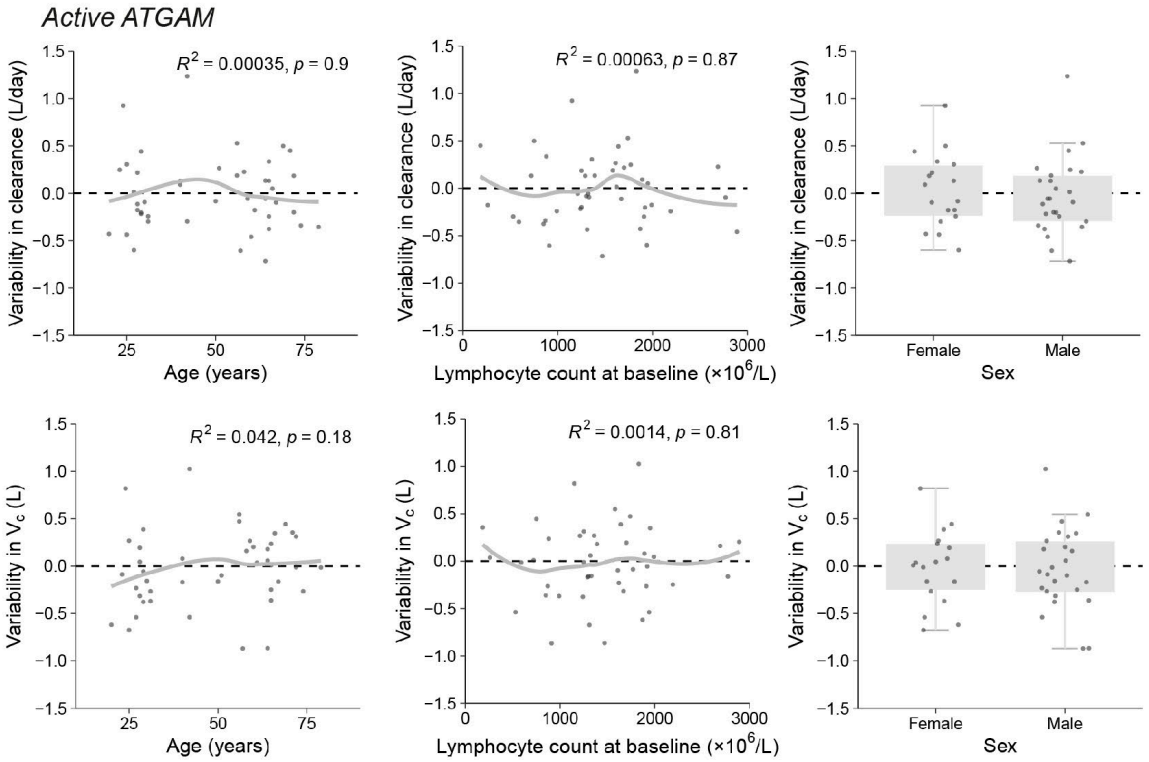

Figure S13. Impact of demographical and clinical covariates on inter-individual variability in pharmacokinetic parameters. Impact of age, lymphocytes pre-ATGAM and sex on inter-individual variability in clearance (row 1) and volume of distribution of the central compartment (row 2) of active ATGAM. Each dot represents a patient.

Figure S14

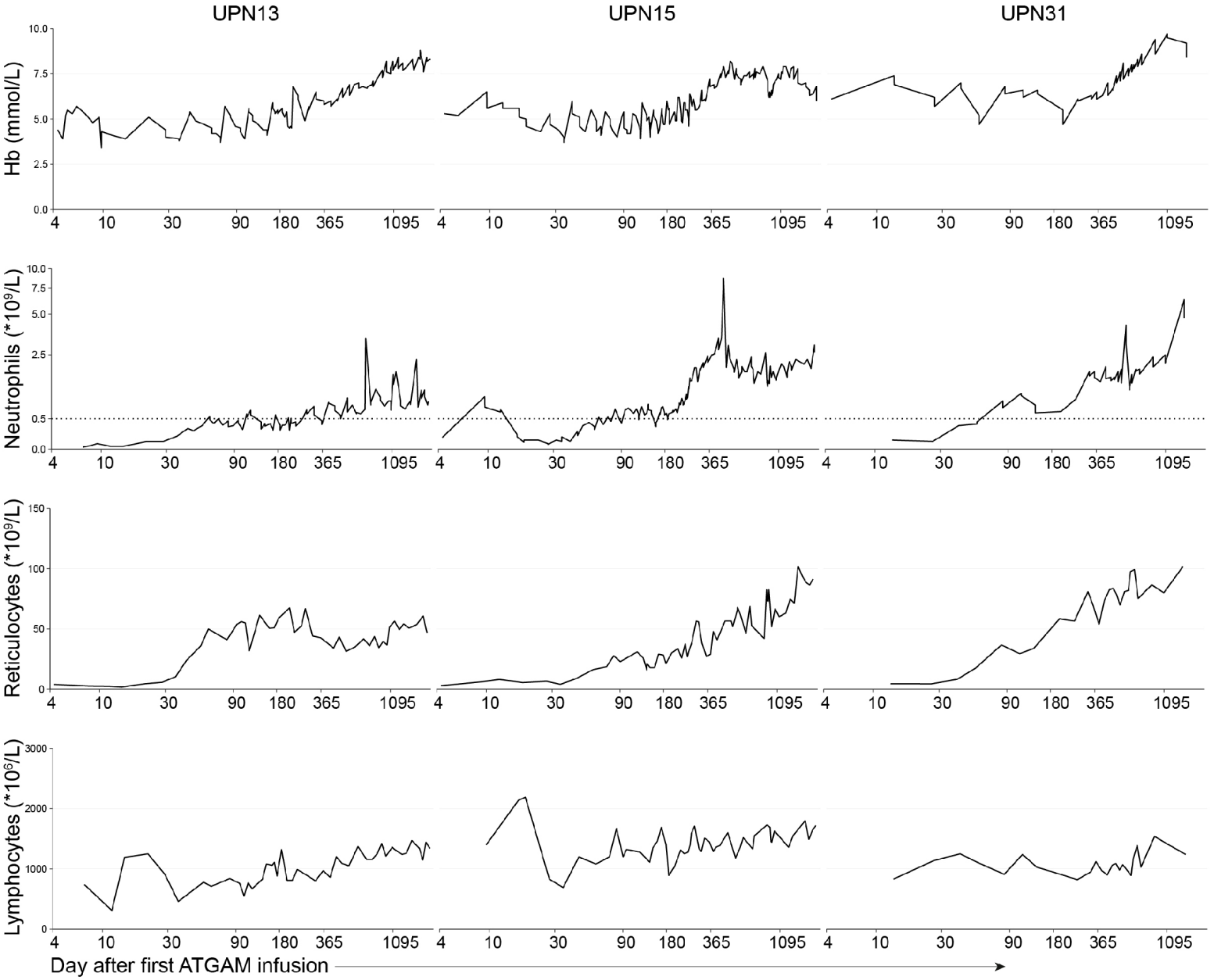

Figure S14. Peripheral blood counts in time after start of ATGAM-based IST. Hemoglobulin (Hb), neutrophil, reticulocyte and total lymphocyte counts in patients UPN13, UPN15 and UPN31 over time, up to 3.5 years after start of ATGAM-based IST.

Figure S15

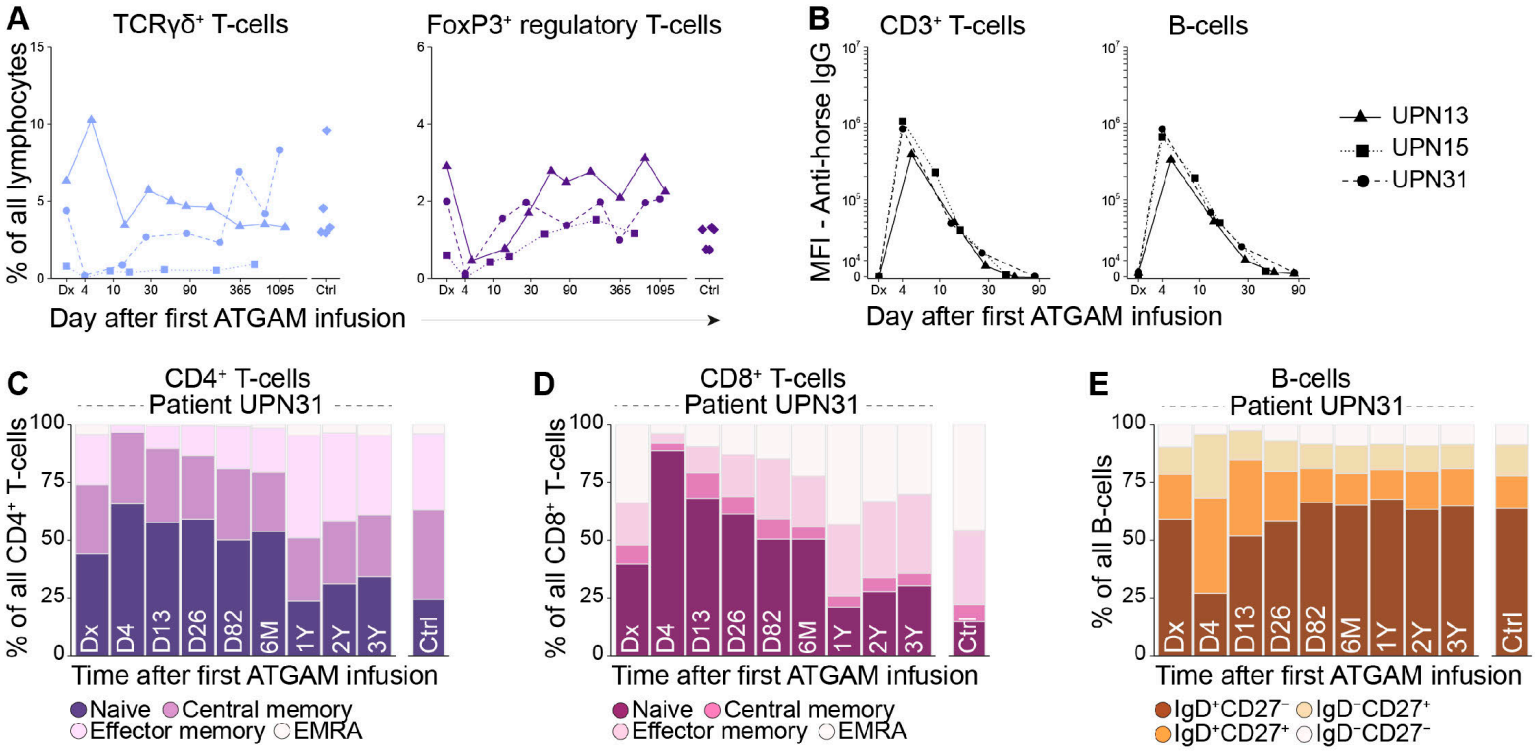

Figure S15. Lymphocyte compartment pre- and over time post-ATGAM. [A] Frequencies of major lymphoid lineages, shown as a percentage of all single, live lymphocytes per time point. Each line represents an individual patient. **[B]** Presence of ATGAM on the cell surface of T-cells (right) and B-cells (left), quantified over time using the mean fluorescence intensity of the Alexa Fluor 488-conjugated anti-horse IgG antibody. Each line represents an individual patient. **[C-E]** Bar plots quantifying the frequencies of subpopulations identified within the CD4⁺ T-cell, CD8⁺ T-cell and B-cell compartments from the representatitive patient UPN31. Flow cytometry plots are shown in Figure 4.

Figure S16

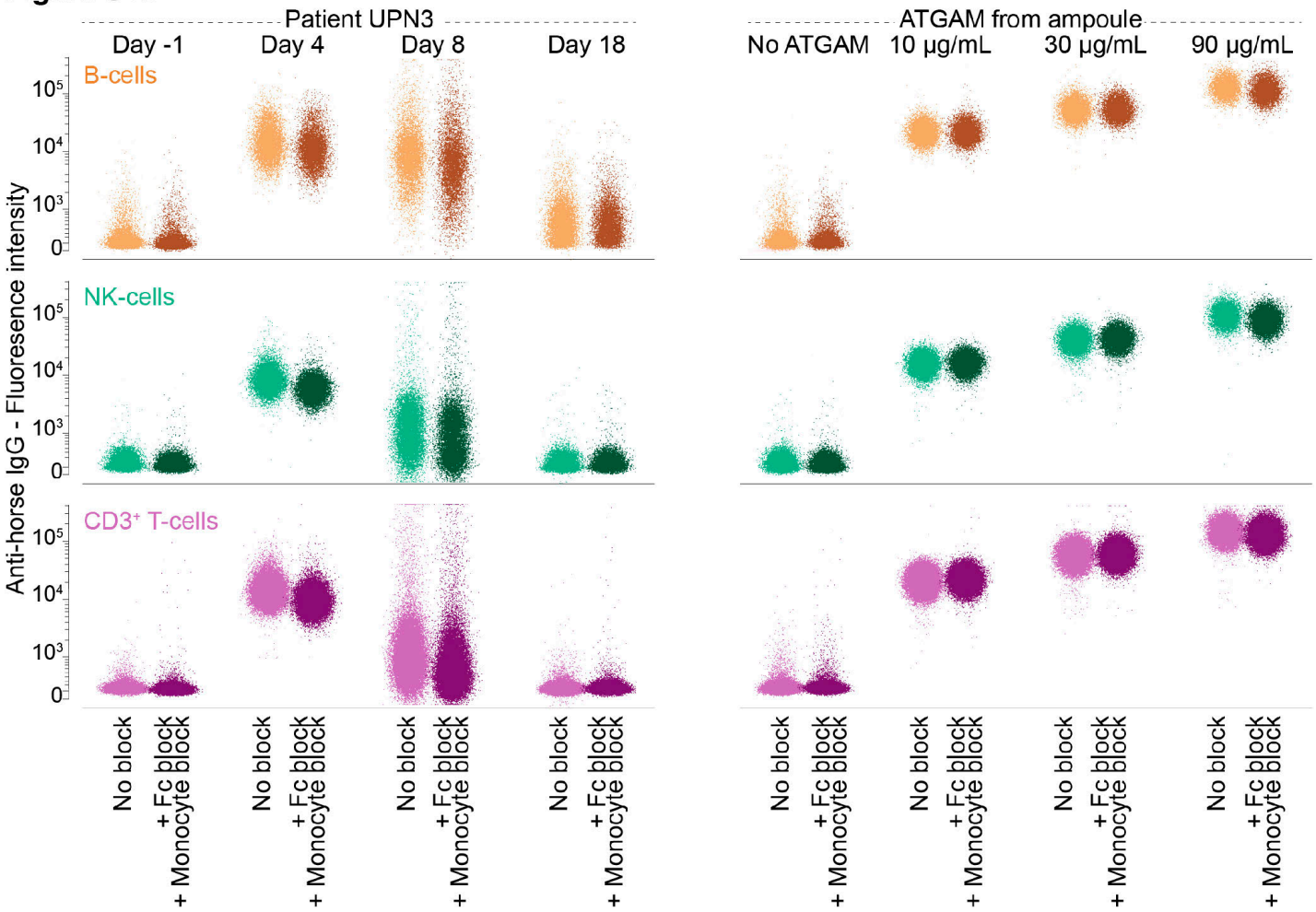

Figure S16. Impact of Fc-receptor blockade on ATGAM binding to lymphoid lineages. PBMCs from a healthy donor were pre-incubated without or with Fc-receptor block (Invitrogen, cat 14-9161-73) and monocyte block (Biolegend, cat 426103) for 30 minutes. Subsequently, cells were washed, co-incubated with undiluted plasma samples collected pre- and post-ATGAM infusion from patient LUMC3 (right), or known ATGAM concentrations (right), and stained as described in the methods section (see 'Quantification of active ATGAM concentrations').

Figure S17

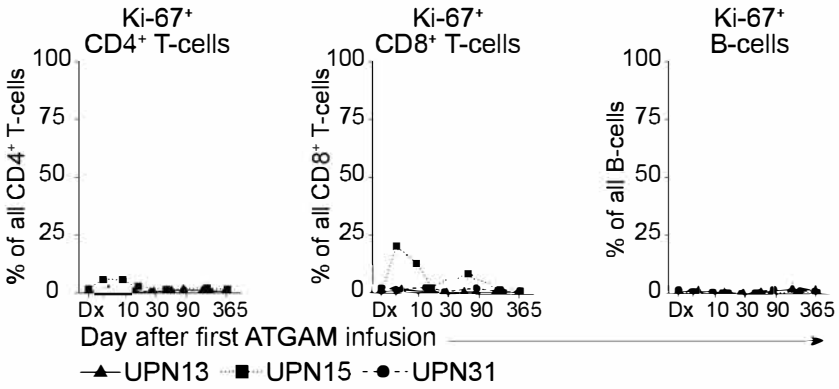

Figure S17. Proliferating CD4+ T-cells, CD8+ T-cells and B-cells after start of ATGAM-based IST. Ki-67+ cells were gated within the CD4+ T-cell, CD8+ T-cell and B-cell compartments. Data are shown for patients UPN13, UPN15 and UPN31.